

**FREE JET EXPANSION LASER SPECTROSCOPY OF  
VAN DER WAALS MOLECULES CONTAINING Ne and Br<sub>2</sub>**

Thesis by  
Barry A. Swartz

In Partial Fulfillment of the Requirements  
for the Degree of  
Doctor of Philosophy

California Institute of Technology  
Pasadena, California

1984

(Submitted September 26, 1983)

• 1984

Barry A. Swartz

All Rights Reserved

**ACKNOWLEDGMENT**

Thanks are extended first of all to my parents, Jerry and Eve Swartz and to my wife, Karen, for their invaluable support. I wish to thank my research advisor, Ken Janda, for the patience he has had with me and for his personal and scientific support. Finally let me make a nowhere near complete list of friends and colleagues with whom I have had the pleasure of being associated here at Caltech: Joe Perry, Brad Anton, David Brinza, Mike Casassa, Colin Western, Francis Celi, David Millar, Richard Scheller, Michael Becker, Kevin Jones, Ahmed Zewail, and the guys in the shop.

**ABSTRACT**

Fluorescence excitation spectra of complexes of Ne and Br<sub>2</sub> containing up to four Ne atoms have been measured. The van der Waals molecules were synthesized in a free jet expansion and excited with tunable excimer-pumped dye laser radiation. Features attributable to van der Waals complexes by virtue of their intensity dependences on molecular beam stagnation pressure appear shifted to the blue of band origins of the  $B^3\Pi_{0g^+} \leftarrow X^1\Sigma_g^+$  transition of all three isotopic species of Br<sub>2</sub>. Spectra were recorded for transitions (11-0) through (30-0) of Br<sub>2</sub> which show that the spectral shifts of the complexes relative to the Br<sub>2</sub> band origins increase with increasing  $v'$ . NeBr<sub>2</sub> shifts range from 5.5 to 8.8 cm<sup>-1</sup>. The spectral widths of the van der Waals features also increase with  $v'$  from a laser bandwidth limited value of 0.10 cm<sup>-1</sup> for NeBr<sub>2</sub> (16-0) to 3.1 cm<sup>-1</sup> for (27-0). This indicates a greater than order of magnitude change in the lifetimes of these complexes with level of vibrational excitation which is discussed in relation to recent theories on the dynamics of weakly bound systems. Estimates of 73 and 64 cm<sup>-1</sup> were obtained for the van der Waals bond dissociation energy for the ground and excited electronic states, respectively.

## TABLE OF CONTENTS

	<u>Page</u>
Introduction .....	2
Experimental .....	11
Results .....	16
Discussion .....	61
APPENDIX I: Design of Optics for Molecular Beam Laser-Induced Fluorescence Experiments .....	73
APPENDIX II: Scanning Electronics for Coherent 699-03 Dye Laser .....	91
APPENDIX III: Design of a Spherical Mirror Fabrey-Perot Interferometer .....	102

**FREE JET EXPANSION LASER SPECTROSCOPY OF  
VAN DER WAALS MOLECULES CONTAINING Ne and Br<sub>2</sub>**

## Introduction

The study of van der Waals molecules has become an important field of interest in recent years.<sup>1</sup> Van der Waals molecules are weakly bound complexes of the type AB-C where AB and C are stable, chemically bound species. Chemical bonds have binding energies of typically 1-10 eV or tens of thousands of wavenumbers. Van der Waals forces, on the other hand, lead to binding energies 100-1000 times weaker than chemical bonds. Dissociation energies for van der Waals bonds typically range from tens to several hundreds of wavenumbers. This means that van der Waals molecules are unstable with respect to collisional dissociation under ambient conditions since  $kT$  at room temperature is  $\sim 200 \text{ cm}^{-1}$ .

Van der Waals forces are important for several reasons. They manifest themselves in many of the bulk properties of gases. For example, they are largely responsible for the non-ideality of gases and are an important factor in transport coefficients.<sup>2</sup> They are also thought to be of major importance in the microscopic mechanistic description of chemical reactions where incipient transition state bond formation and breakage may have considerable van der Waals character. Van der Waals forces also play a large role in dictating the overall structure of biological macromolecules. More recently, van der Waals molecules have been scrutinized because of their applicability to the study of intramolecular energy transfer and vibrational predissociation. Consider the following reaction:



Excess vibrational energy in the chemically bound moiety AB\* of the van der Waals complex finds its way in a characteristic time  $\tau$  into the van der Waals bond, leading to predissociation of the complex. Any excess of energy between the initial vibrational excitation and the bond dissociation energy is left as relative kinetic energy of the products. Much of the interest in these types of processes is spurred on by the fact that these predissociation lifetimes,  $\tau$ , can vary over many orders of magnitude. Casassa et al. have witnessed dissociation lifetimes of  $\sim 10^{-13}$  s for dimers of ethylene vibrationally excited with infrared radiation, while at the other extreme, Ewing has calculated a predissociation lifetime of  $\sim 10^{10}$  s for HF bound to a crown ether.<sup>4</sup>

Van der Waals molecules have been traditionally investigated through studies of bulk properties. However, while a detailed description of a microscopic force may be straightforwardly averaged to yield an adequate description of a bulk property, the reverse process is not usually possible. In addition, bulk properties are usually only sensitive to the repulsive and long range parts of the intermolecular potential curves leaving the portion of the well around the minimum largely undetermined. Thus, it is necessary to try to prepare van der Waals molecules under conditions where they are bound for appreciable lengths of time in order that spectroscopy may be done on these complexes to gain information about their binding and dissociation dynamics.

Several approaches have been taken to spectroscopically observe van der Waals complexes. First, unusually strongly bound complexes of molecules with very strong spectroscopic transitions have been studied. Examples of

this approach are the infrared spectra of the dimers of HF and HCl<sup>5</sup> where the combination of very strong vibration-rotation bands and the partial hydrogen bonding character of the van der Waals bond have allowed their observation in static gas samples. Another approach has been to use very long absorption path lengths in gases at low temperature. Here the equilibrium concentration of van der Waals complexes is relied on for the signal. This technique has been used to observe spectra of H<sub>2</sub>Ar,<sup>6</sup> N<sub>2</sub>Ar,<sup>7</sup> O<sub>2</sub>Ar,<sup>8</sup> (O<sub>2</sub>)<sub>2</sub><sup>9</sup> and (N<sub>2</sub>)<sub>2</sub><sup>10</sup> as well as other complexes. Much of this data is very good, with the potential surface of H<sub>2</sub>Ar being the most completely determined van der Waals potential surface to date. These studies have pointed out the important consideration that although spectroscopy yields the best information on van der Waals complexes, low pressures must be used since the studies cannot tolerate broadening. This is due to the fact that the rotational constants for van der Waals molecules are generally small because of the long bond lengths in these weakly bound complexes. The third approach taken in recent years to doing van der Waals molecule spectroscopy has been to study systems which are not in thermodynamic equilibrium.

To achieve non-equilibrium state distributions, van der Waals molecules have been synthesized in supersonic expansions of appropriate gas mixtures.<sup>11</sup> A gas at initial pressure  $P_0$  and temperature  $T_0$  is expanded into a vacuum through a nozzle with diameter  $D$  to a final lower temperature  $T_1$  and pressure  $P_1$ . The expansion can be easily made to be isentropic where random thermal enthalpy in the static gas behind the nozzle is converted to directed mass flow downstream from the nozzle. The initial translational energy distribution which is centered on 0 velocity and has a width

determined by  $T_0$  is both shifted and narrowed to a width determined by  $T_1$ . Thus, although the flow velocity is large, the relative kinetic energy of molecules in the expansion is low and can lead to the formation of van der Waals complexes in the expansion via low energy collisions.

The expansion would simply result in the chilling of the expansion mixture except for the fact that as the gas flows downstream from the nozzle it becomes rarefied. As the gas expands it eventually reaches a point where collisions are no longer probable. After reaching the collision-free region a molecule is isolated from the surrounding gas such that the state distribution determined in the collisional region of the expansion is frozen in. Thus, the kinetics of the expansion dominate over thermodynamics and degrees of freedom which equilibrate slowly with translation will be far from thermodynamic equilibrium.

Rotational motion equilibrates rather rapidly with translation so the molecules in the collision free region show rotational state distribution with characteristic low temperatures. The same effect occurs for molecular vibrations to a lesser extent. Complex formation, however, is relatively slow so that under appropriate expansion conditions, stable van der Waals molecules may be formed without complete condensation of the expanding gas.

The kinetics of complex formation are often complicated. The synthesis of specific van der Waals molecules has thus been largely accomplished through empirical variation of the expansion conditions. The variable parameters available to the experimenter are the initial pressure and temperature, the final temperature (chosen by selecting the downstream

position where the expansion is analyzed), the carrier gas and the concentration of the reactants.

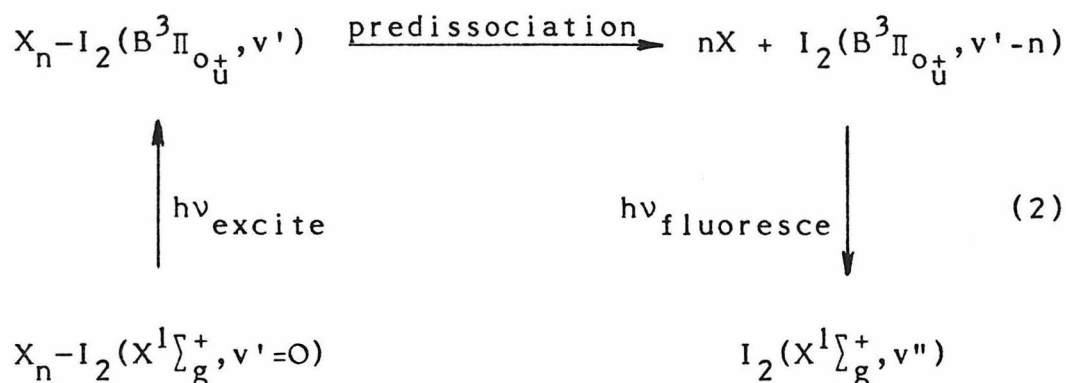
Several groups have employed various spectroscopic techniques to analyze van der Waals molecules prepared in supersonic expansions. Klemperer and coworkers have determined accurate ground state constants for many van der Waals molecules using the technique of electric resonance to measure their radio frequency spectra. Some of the molecules they have studied are ArHCl,<sup>12</sup> ArHF,<sup>13</sup> ArClF,<sup>14</sup> KrClF<sup>15</sup> and HF-ClF.<sup>16</sup> Similarly, Howard and coworkers have used electric resonance experiments to take microwave spectra of species such as (NO)<sub>2</sub>.<sup>17</sup>

Janda's group has studied the predissociation dynamics of complexes containing ethylene using the technique of infrared photodissociation.<sup>3,18</sup> Here, a vibrational mode in the ethylene moiety of complexes of ethylene bound to rare gases or other ethylene molecules is excited by bathing the complexes in CO<sub>2</sub> laser radiation and looking for the resulting loss in mass spectrometer signal as the complexes dissociate.

Bolometer detection has been employed by another group<sup>19</sup> to measure infrared spectra of van der Waals molecules formed in supersonic expansions.

Levy and coworkers have pioneered the use of optical techniques in the analysis of van der Waals molecules formed in supersonic expansions. In addition to studying such molecules as NaAr,<sup>20</sup> they have conducted an in depth analysis of molecules containing I<sub>2</sub> and rare gas atoms.<sup>21-28</sup> They have used the technique of laser fluorescence excitation spectroscopy where the exciting laser wavelength is scanned while monitoring the total induced fluorescence to obtain structural and lifetime information for many I<sub>2</sub>-rare

gas molecules. Additionally, they have dispersed the fluorescence resulting from laser excitation of these complexes to yield values for the van der Waals binding energies as well as further insight into the dynamics of the predissociation process in these species. The following dynamical scheme has been observed for I<sub>2</sub>-rare gas complexes:



where X is one or more of the rare gas atoms He, Ne, Ar, or H<sub>2</sub> or D<sub>2</sub>. After vibronic excitation, the complexes contain more than enough vibrational energy to dissociate the van der Waals bond. This predissociation process has been determined from linewidth measurements to occur on the time scale of tens to hundreds of picoseconds, depending on the level of vibronic excitation. This is orders of magnitude faster than the  $\mu$ sec fluorescence lifetime of I<sub>2</sub> so all fluorescence is detected from the free I<sub>2</sub> fragment following predissociation. The vibrational energy content of the I<sub>2</sub> predissociation fragment has been found to reveal, for all but the largest complexes, the loss of one vibrational quantum per rare gas atom dissociated. This one-to-one propensity rule is found to hold for vibronic excitation to lower v' levels. However, at sufficiently high vibrational levels the energy of

the  $I_2$  vibrational quanta are less than the dissociation energy of the van der Waals bond. Here, the onset of multiple quanta predissociation channels is observed. This transition from one to two quantum channels has been used to bracket the dissociation energy of the van der Waals bond within the anharmonicity of the  $I_2$  stretching vibration. Values range from  $\sim 14$   $cm^{-1}$  for  $HeI_2$  to  $\sim 255$   $cm^{-1}$  for  $ArI_2$ . Fluorescence excitation spectra of  $HeI_2$  indicate that the complex has a T shaped equilibrium structure.

Similar results have been obtained in our laboratory for  $NeCl_2$ <sup>29</sup> from fluorescence excitation spectra. Here, the predissociation rate in the ground electronic state was slow enough to also observe  $NeCl_2$  bands associated with the  $v'' = 1$  vibrational level. Efforts to observe analogous bands in  $I_2$  resulted in the assumption that  $I_2$ -rare gas molecules in supersonic expansions predissociate before reaching the region of laser excitation.<sup>2,24,27</sup> Again, a T shape structure was indicated for  $NeCl_2$ .

This thesis reports fluorescence excitation spectra of complexes of Ne and  $Br_2$ . As has been the case for  $I_2$ -rare gas and  $NeCl_2$  complexes, bands associated with  $Ne_nBr_2$  have been observed slightly blue shifted from  $Br_2$  vibronic bands. Again,  $v'$  dependent predissociation rates have been observed from linewidths measured by scanning the exciting laser wavelength and monitoring the total fluorescence emitted by the resultant  $Br_2$  fragments.

Several workers have theoretically treated van der Waals molecules. LeRoy<sup>30</sup> has done extensive close-coupling calculations to determine the shapes of potential energy surfaces as well as to calculate rotational energy levels and analyze the dynamics of rotational predissociation processes. The problem of vibrational predissociation in van der Waals molecules has been

addressed by Ewing<sup>4,31</sup> and by Jortner and coworkers.<sup>32-35</sup> Ewing<sup>36</sup> has advanced a momentum gap law to account for the large range of rates of vibrational predissociation observed for van der Waals complexes. He has used a Fermi's golden rule expression,

$$\tau^{-1} = (4/\hbar^2 v_f) |\langle \Psi_f | V | \Psi_i \rangle|^2 \quad (3)$$

where the initial wave function,  $\Psi_i$ , is a Gaussian function describing the  $v = 0$  level of the van der Waals stretching mode and the final state,  $\Psi_f$ , is a rapidly oscillating function corresponding to the free particle plane wave of the fragments with deBroglie wavelength  $\lambda = h/p$ . The coupling Hamiltonian,  $V$ , is shown to be a slowly varying function of the internuclear separation. Ewing has found the predissociation rate to vary as a function of the momentum

$$p = (2\mu_v \Delta E)^{1/2} \quad (4)$$

where  $\mu_v$  is the reduced mass of the complex and  $\Delta E$  is given by

$$\Delta E = W_{AB} - D_0 \quad (5)$$

where  $W_{AB}$  is the energy of the vibrational quanta of the chemically bound species  $AB$  and  $D_0$  is the dissociation energy of the van der Waals bond. For near matches of the vibrational energy,  $W_{AB}$ , and the dissociation energy,

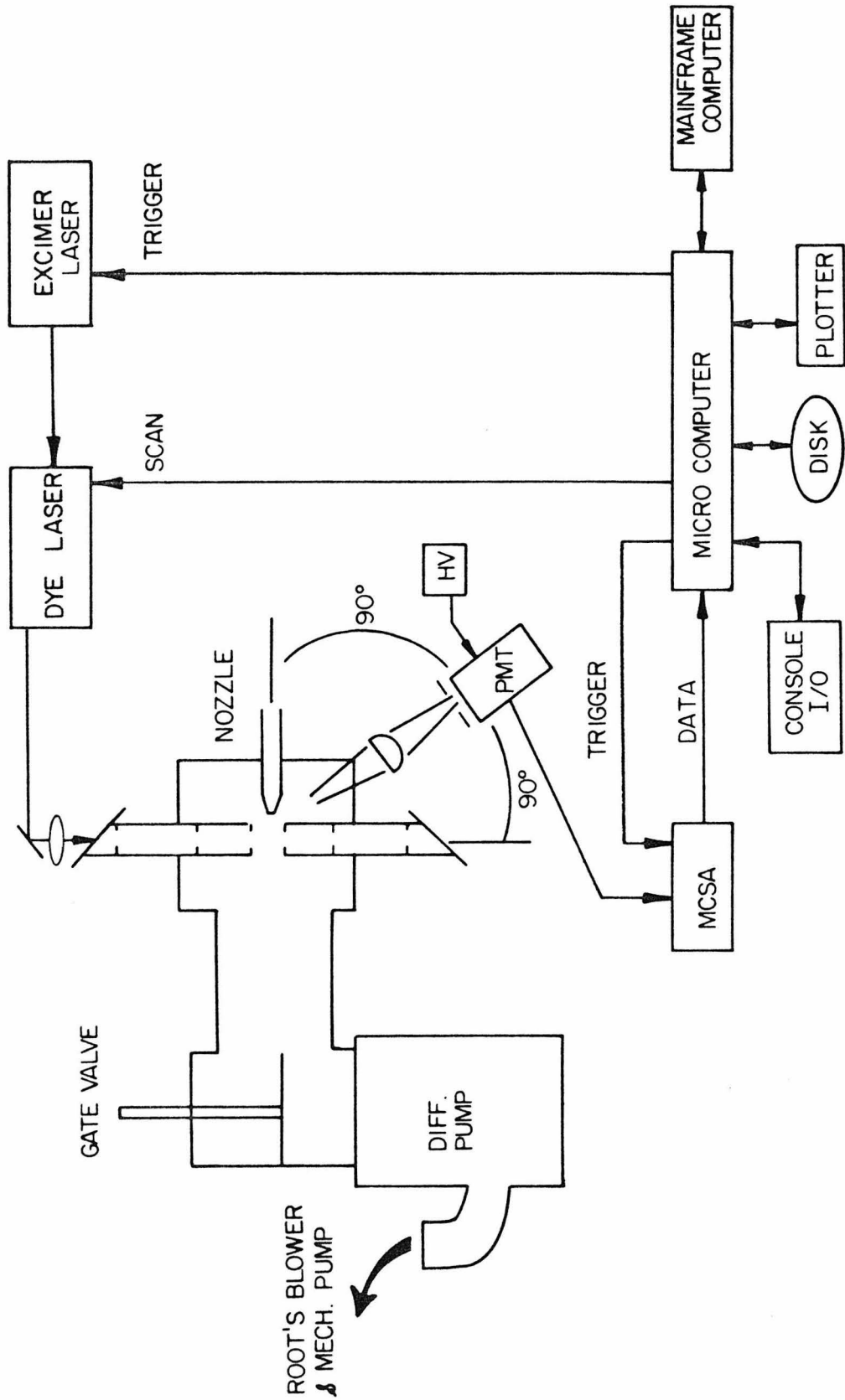
$D_0$ , the lifetime of the complex is short while if  $\Delta E$  and thus  $p$  is large, the predissociation is slow. This can be seen to intuitively follow from Equation 3. If the fragments leave with large momentum then  $\Psi_f$  will oscillate rapidly and have poor integrated overlap with the Gaussian function  $\Psi_i$ . On the other hand, if  $\Delta E$  is small and thus  $\Psi_f$  oscillates slowly, then the integral in Equation 3 will be large and the predissociation lifetime short. Jortner<sup>33</sup> has similarly derived an energy gap law for the specific case of  $I_2$ -rare gas molecules and has done a number of calculations using various approximations to the potential energy curves in calculating  $\Psi_i$  and  $\Psi_f$  and defining  $V$ .

## Experimental

Fluorescence excitation spectra were measured using the instrument schematically diagrammed in Figure 1. A 10,000  $\ell/s$  16" diffusion pump, roughed with a 47,000  $\ell/s$  Roots blower and mechanical pump, pumps the 19" cubic spectroscopy chamber through a 20" gate valve and a 2' long 16" diameter channel. Van der Waals molecules were synthesized by expanding gas mixtures at pressures up to 300 psi through a 30  $\mu$  quartz nozzle into the chamber. Background pressures were less than one mtorr at the highest stagnation pressures. The nozzle was constructed by drawing 2 mm ID 8 mm OD quartz tubing to a tapered sealed end. This end was then ground to create a hole by spinning the quartz tube against fine sandpaper using a drill press. The grinding was halted the moment methyl alcohol, which had been placed in the tube, began to leak through the newly formed orifice. The nozzle was tested on a vacuum chamber equipped with a mass spectrometer to insure that beams of argon were emitted straight and provided adequate cooling to allow detection of a large argon dimer signal.

Expansion mixtures of rare gases seeded with bromine were created by passing the noble gases over bromine which was contained in a stainless steel u-tube. The u-tube was immersed in a carbon tetrachloride dry ice bath at  $-23^{\circ}\text{C}$ . This resulted in the beam carrying an equilibrium vapor pressure of 10.8 torr  $\text{Br}_2$ . It was empirically determined that this partial pressure of bromine gives the appropriate amount of cooling in the expansion to create the most van der Waals molecules of neon and bromine. It was also found that rare gas mixtures of helium and neon produced the highest concentrations of van der Waals molecules of neon and bromine when the

**Figure 1.** Apparatus used to record fluorescence excitation spectra of species in supersonic free jet expansions.



neon concentration was highest. Therefore, an inexpensive mixture of 90% Ne and 10% He (Scientific Gases) was used for nearly all the experiments. Reagent grade bromine (J. T. Baker, assay 100.0%) was used without further purification.

The molecules in the free expansion were excited approximately 0.5 cm downstream of the nozzle by a pulsed laser beam. The laser source is an excimer pumped dye laser (Lamda Physik FL 2002) which is grating tuned and has a bandwidth ranging from 0.23 to 0.33  $\text{cm}^{-1}$  over the wavelength range 521 to 574 nm which is covered by the dye Coumarin 540. The pump laser is a Lumonics 861-S operated on xenon chloride with a pulse energy of 90 mJ and duration of 5 nsec. The maximum repetition rate is 30 Hz. This results in dye laser pulses of 10 mJ and 4.5 n sec which are focused by a 50 cm focal length lens through a fused silica Brewster's angle window into the center of the vacuum chamber. Baffle tubes reduce scattered light. Known vibronic bands of bromine served to calibrate the laser.<sup>37,38</sup>

Fluorescence was collected by means of a 50 mm focal length aspheric condenser lens with f-number equal to 0.7. The fluorescence region was imaged on a set of two dimensional slits which serve to reject scattered light and pass the selected portion of the fluorescence region to the immediately following photomultiplier tube detector (RCA 7265). A color filter could be placed in front of the phototube. The fluorescence collection and detection assembly is translatable along the beam axis and the nozzle is movable in three dimensions so that any portion of the free expansion may be analyzed at or downstream of the volume of intersection with the focused laser beam.

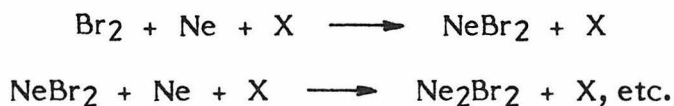
The photomultiplier tube current signal was measured using a multi-

channel signal averager. A microcomputer triggered the laser and signal averager. Channels corresponding to long times after the laser pulse were subtracted from channels corresponding to times overlapping the laser pulse to remove background. The computer also stepped the dye laser wavelength, summed the signal from an adjustable number of laser shots, and stored the resulting spectra on flexible discs.

## Results

Figure 2 shows a portion of the fluorescence excitation spectrum of the free jet expansion of a mixture containing ~0.1% Br<sub>2</sub> in 90% Ne and 10% He. The most intense features are due to the (21-0) vibronic bands of the B<sup>3</sup>Π<sub>o<sub>u</sub> ← X<sup>1</sup>Σ<sub>o<sub>g</sub> transition in the three isotopic species of molecular bromine. In addition, the (25-1) bands of <sup>79</sup>Br<sup>81</sup>Br and <sup>79</sup>Br<sub>2</sub> are observed coinciding with the <sup>81</sup>Br<sub>2</sub> (21-0) band and a feature assigned to Ne<sup>81</sup>Br<sub>2</sub>, respectively. The other three peaks in the spectrum have also been assigned to van der Waals complexes of neon and bromine. Figure 3 shows an extension to higher frequency of the spectral scan of Figure 2. Again, the intense peak originates from molecular bromine. The weaker features which generally decrease in intensity towards the blue end of the spectrum are due to complexes containing Br<sub>2</sub> and increasing numbers of Ne atoms.</sub></sub>

In making the assignments of Ne<sub>n</sub>Br<sub>2</sub> (n = 1-4) bands, their intensity relative to the intensity of the corresponding Br<sub>2</sub> bands as a function of nozzle stagnation pressure was examined. Figure 4 shows this pressure dependence for the Ne<sup>79</sup>Br<sup>81</sup>Br, Ne<sub>2</sub><sup>81</sup>Br<sub>2</sub>, and Ne<sub>2</sub><sup>79</sup>Br<sup>81</sup>Br features associated with the Br<sub>2</sub> (21-0) vibronic bands. Complex formation in a free expansion proceeds by one or more of the following steps:



Here, the collision of the species X is necessary to remove as kinetic energy the binding energy of the complex. Although the P<sup>2</sup> and P<sup>4</sup> dependences

**Figure 2.** Fluorescence excitation spectrum of the (21-0) band of the  $B^3\Pi_{0u}^+ \leftarrow X^1\Sigma_g^+$  optical transition in  $Br_2$  and associated van der Waals complexes in a free jet expansion. Expansion conditions are tabulated in the figure. The nozzle was held at room temperature. A Schott OG 570 color filter was used to reduce scattered laser light. Note that in this scan the  $Br_2$  bands are slightly saturated.

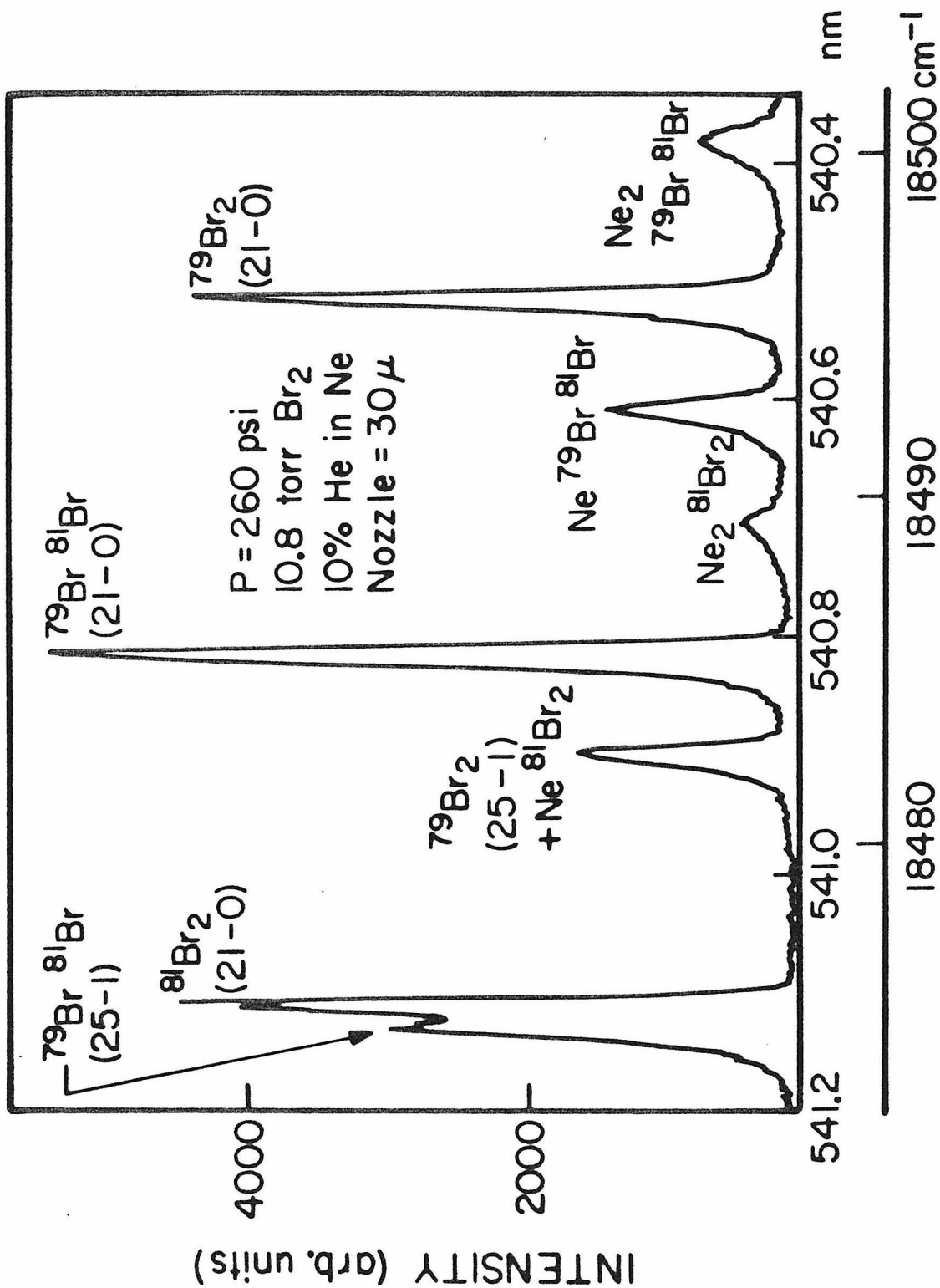
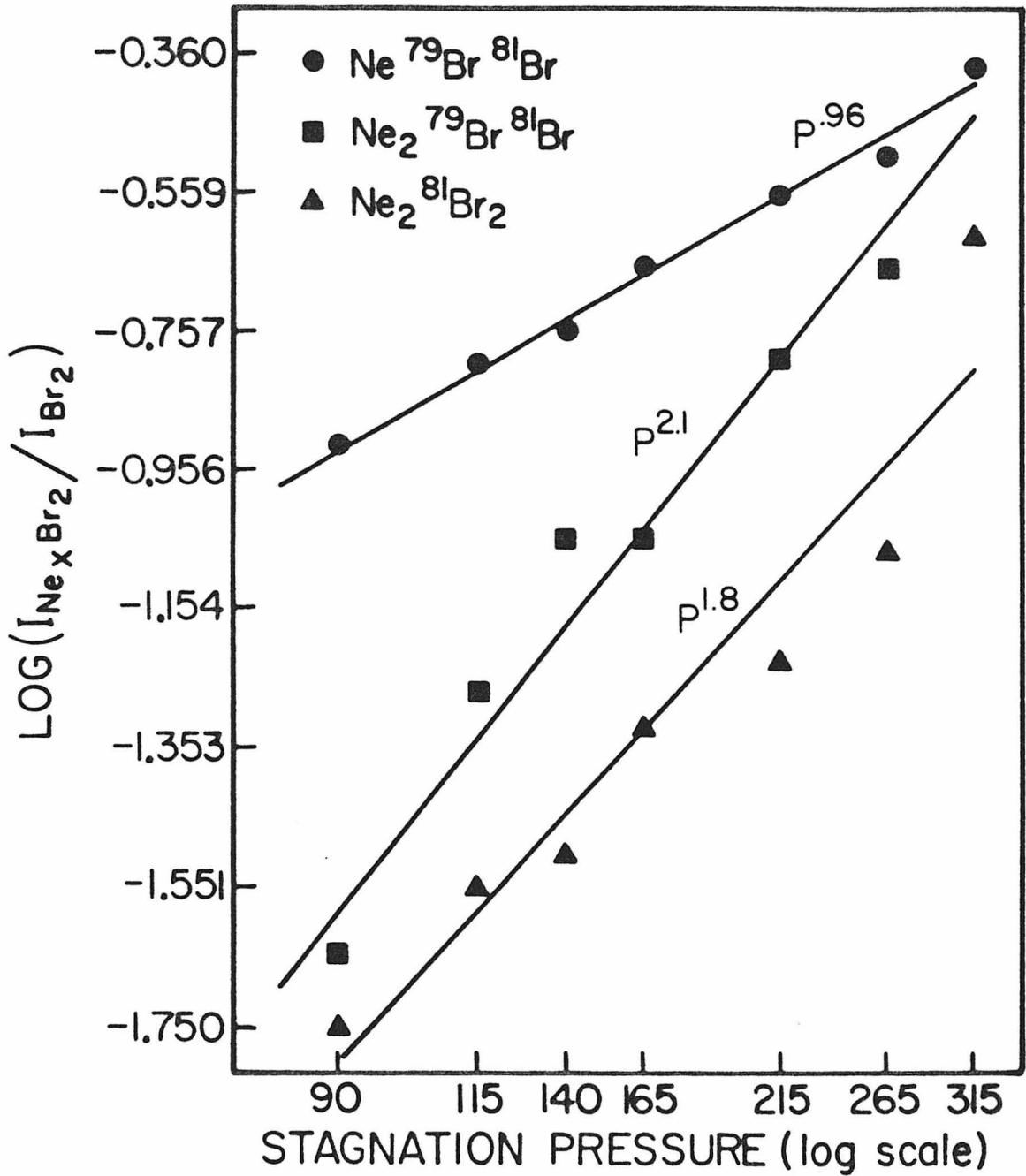


**Figure 3.** Fluorescence excitation spectrum of the (21-0) vibronic band of  $^{79}\text{Br}_2$  and van der Waals features appearing to the blue of this band. A Schott OG 570 color filter was used.



**Figure 4.** Nozzle stagnation pressure dependence of the integrated band intensities of (21-0) NeBr<sub>2</sub> and Ne<sub>2</sub>Br<sub>2</sub> bands relative to Br<sub>2</sub> band intensities.



expected for NeBr<sub>2</sub> and Ne<sub>2</sub>Br<sub>2</sub> complex formation are not fully realized, the fact that the Ne<sub>2</sub>Br<sub>2</sub> band pressure dependences are approximately two orders stronger than that for NeBr<sub>2</sub> (which itself is enhanced relative to the Br<sub>2</sub> bands at higher pressures) implies that the assignments are valid. An explanation for these weaker pressure dependences may be the occurrence of the following types of reactions in the expansion:



where Ne<sub>2</sub> should be present in the jet since it is bound by  $\sim 30 \text{ cm}^{-1}$ .<sup>39</sup> Further evidence for the assignments is the fact that all spectral features assigned to complexes of Ne and Br<sub>2</sub> were absent in spectra taken of expansions of Br<sub>2</sub> in pure helium. In addition, the relative intensity of these same features proved insensitive to changes in the Br<sub>2</sub> concentration in the expansion mixture. These results exclude the possibility that complexes containing only bromine, i.e. (Br<sub>2</sub>)<sub>n</sub>, are responsible for the observed spectral features.

Still further evidence supporting the Ne<sub>n</sub>Br<sub>2</sub> assignments (as opposed to their being due to an impurity) lies in the fact that these features are found associated with all three Br<sub>2</sub> isotopic bands (with the appropriate  $\sim 1:2:1$  intensity distributions) of each vibronic level from (11-0) to (30-0). Failure to observe complexes associated with bands with  $v' \leq 10$  is presumably due to the low signal levels which result from poor Franck-Condon factors at low  $v'$ . Spectral congestion prevented extending the study to higher  $v'$  levels.

All van der Waals features appear blue shifted with respect to their associated molecular bromine bands. For a given vibronic band, the shift per Ne atom bound in the complex is approximately constant. That is, the shift of  $\text{Ne}_2\text{Br}_2$  is approximately twice that for  $\text{NeBr}_2$ , etc. However, the spectral shift per Ne atom increases with  $v'$ . This can be seen by comparing Figure 5 with Figure 2. Figure 5 displays the spectral region containing the (14-0)  $\text{Br}_2$  vibronic bands and associated van der Waals features where a shift per neon atom of  $\sim 6 \text{ cm}^{-1}$  is observed while a shift of  $\sim 7 \text{ cm}^{-1}$  is found for the (21-0) band in Figure 2. A complete tabulation of all measured shifts for complexes of Ne and  $\text{Br}_2$  is given in Table I. The absence of data for some isotopic vibronic bands is caused by coincidences of complex bands with  $\text{Br}_2$  hot bands, or, for higher  $v'$ , with other isotopic bands of the same vibronic transition. These data are displayed graphically in Figure 6.

The shapes of vibronic bands of  $\text{Br}_2$  were analyzed to determine the rotational temperature of molecules in the supersonic expansion. Known rotational constants and band origins for  $\text{Br}_2$ <sup>37,38</sup> were input to a program which calculates diatomic molecular spectra. Again, comparing Figure 2 and Figure 5 it is obvious that the resolution of the bromine bands is not constant but varies with wavelength due to the changing laser bandwidth. Therefore, the program was made to include a convolution routine which accounted for the finite excitation bandwidth in the calculated bandshapes. The rotational level population distribution was assumed to be Boltzmann, with characteristic temperature  $T_{\text{rot}}$ . A non-linear least squares fitting routine was used to vary the rotational temperature, laser bandwidth, and absolute wavelength correction to achieve agreement with the measured bandshape. This provided

**Figure 5.** Fluorescence excitation spectra of the (14-0) vibronic band of Br<sub>2</sub> and associated van der Waals features. A Schott OG 590 color filter was used.

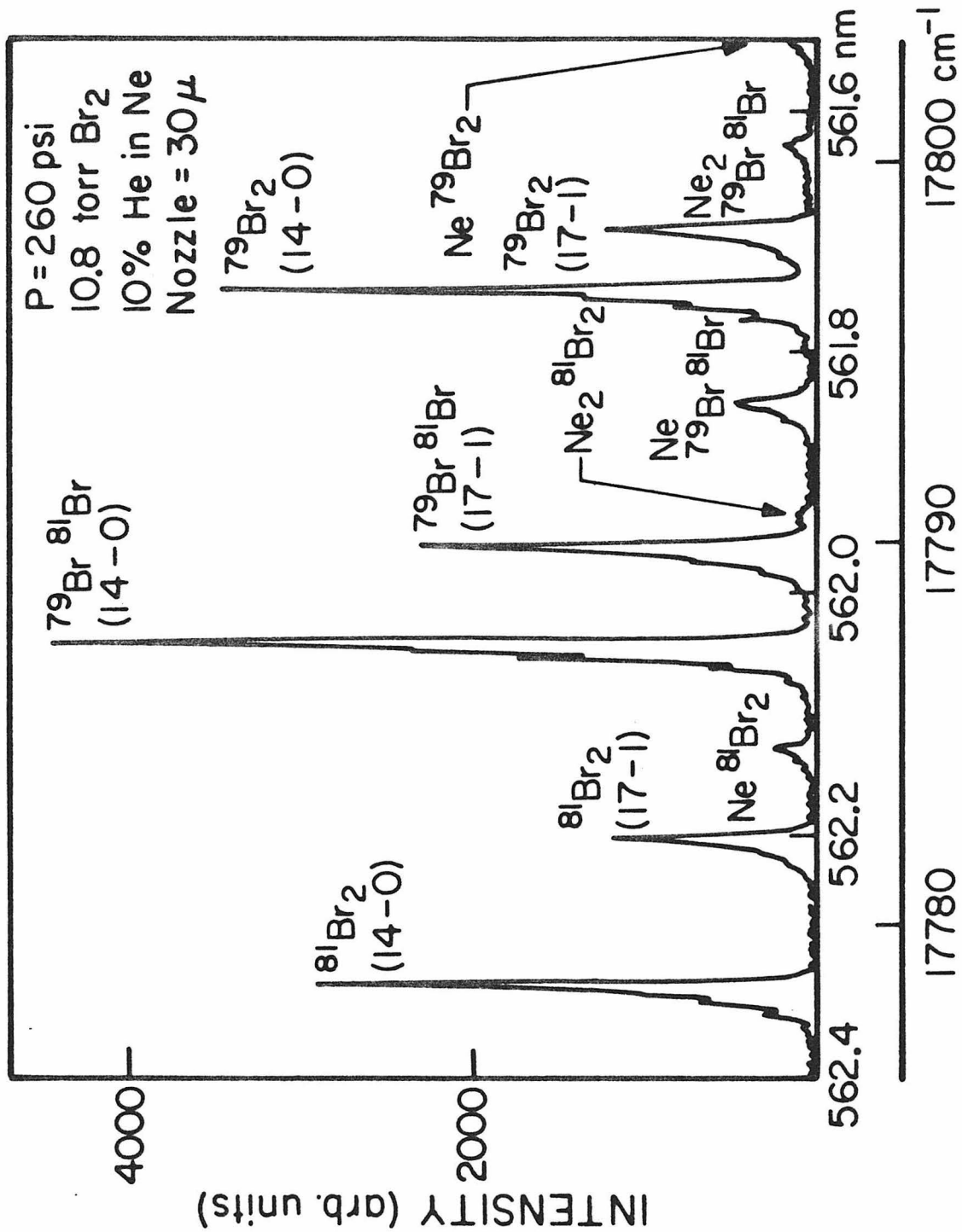


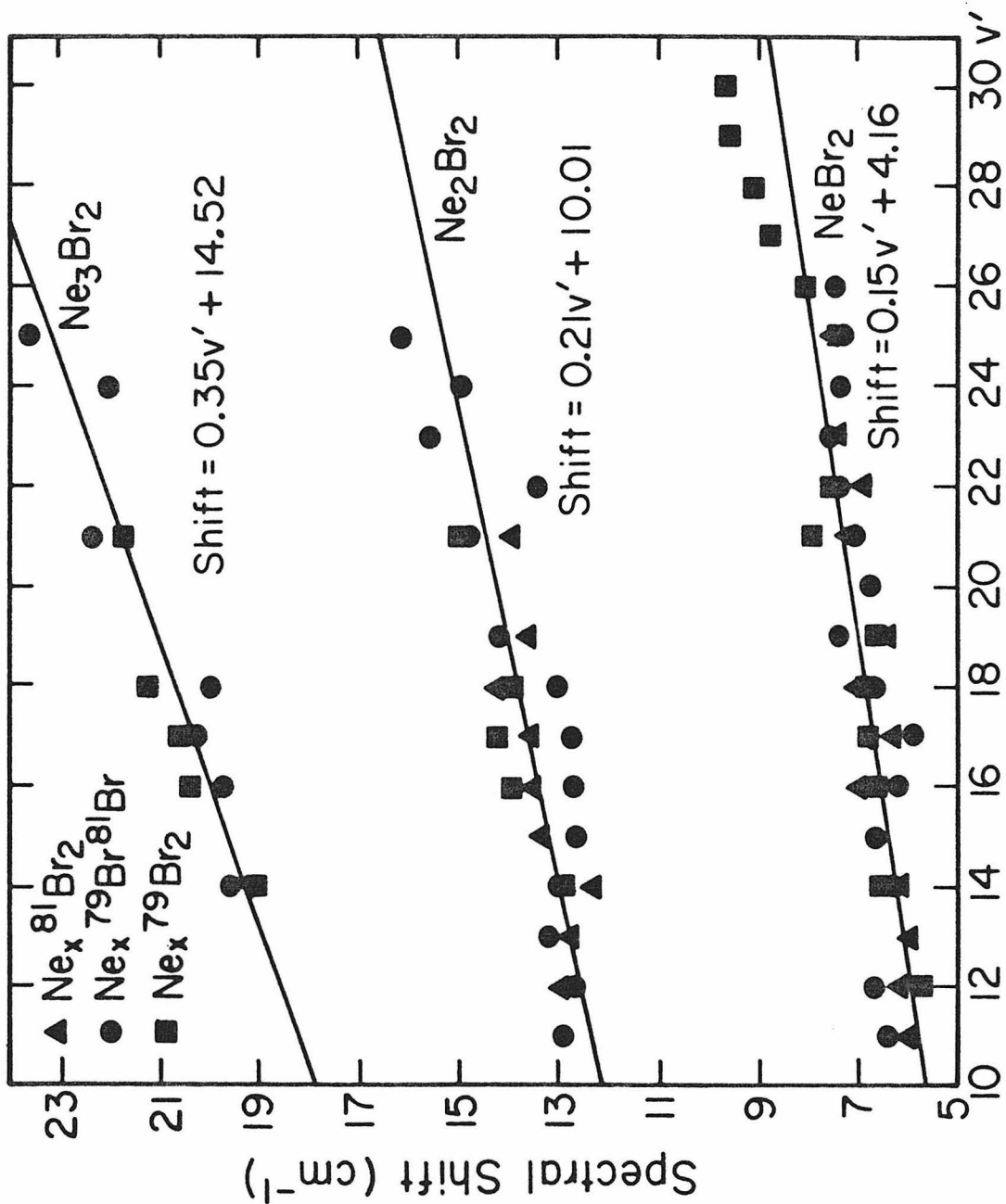
**Table I.** Spectral blue shifts in  $\text{cm}^{-1}$  of van der Waals complexes relative to their respective  $\text{Br}_2$  bands.

$\nu'$	$\text{Ne}^{\delta 1}\text{Br}_2$	$\text{Ne}^{79}\text{Br}_2$	$\text{Ne}^{79}\text{Br}^{\delta 1}\text{Br}$	$\text{Ne}_2^{\delta 1}\text{Br}_2$	$\text{Ne}_2^{79}\text{Br}_2$	$\text{Ne}_2^{79}\text{Br}^{\delta 1}\text{Br}$	$\text{Ne}_3^{79}\text{Br}_2$	$\text{Ne}_3^{79}\text{Br}^{\delta 1}\text{Br}$	$\text{Ne}_4^{79}\text{Br}^{\delta 1}\text{Br}$
11	6.03	--	6.44	--	--	12.93	--	--	--
12	6.21	5.70	6.72	12.93	--	12.64	--	--	--
13	6.06	--	--	12.78	--	13.20	--	--	--
14	6.16	6.59	6.36	12.33	12.83	12.95	19.07	19.61	--
15	--	--	6.67	13.34	--	12.61	--	--	--
16	7.01	6.66	6.22	13.53	13.96	12.67	20.40	19.74	--
17	6.39	6.82	5.90	13.52	14.29	12.77	20.64	20.26	--
18	7.07	6.74	6.67	14.29	14.00	13.00	21.26	20.01	--
19	6.44	6.52	7.39	13.60	--	14.21	--	--	--
20	--	--	6.73	--	--	--	--	--	--
21	7.20	7.97	7.15	13.98	14.95	14.82	21.78	22.44	29.28

Table I. Continued.

$v'$	Ne <sup>81</sup> Br <sub>2</sub>	Ne <sup>79</sup> Br <sub>2</sub>	Ne <sup>79</sup> Br <sup>81</sup> Br	Ne <sub>2</sub> <sup>81</sup> Br <sub>2</sub>	Ne <sub>2</sub> <sup>79</sup> Br <sub>2</sub>	Ne <sub>2</sub> <sup>79</sup> Br <sup>81</sup> Br	Ne <sub>2</sub> <sup>79</sup> Br <sup>81</sup> Br <sup>81</sup> Br	Ne <sub>3</sub> <sup>79</sup> Br <sub>2</sub>	Ne <sub>3</sub> <sup>79</sup> Br <sub>2</sub> <sup>81</sup> Br	Ne <sub>3</sub> <sup>79</sup> Br <sub>2</sub> <sup>81</sup> Br <sup>81</sup> Br	Ne <sub>4</sub> <sup>79</sup> Br <sup>81</sup> Br
22	6.90	7.50	7.30	--	--	13.42	--	--	--	--	--
23	7.43	--	7.54	--	--	15.55	--	--	--	--	--
24	--	7.65	7.35	--	--	14.97	--	22.01	--	--	--
25	7.51	7.38	7.30	--	--	16.15	--	23.62	--	--	--
26	--	8.01	7.40	--	--	--	--	--	--	--	--
27	--	8.80	--	--	--	--	--	--	--	--	--
28	--	9.10	--	--	--	--	--	--	--	--	--
29	--	9.59	--	--	--	--	--	--	--	--	--
30	--	9.62	--	--	--	--	--	--	--	--	--

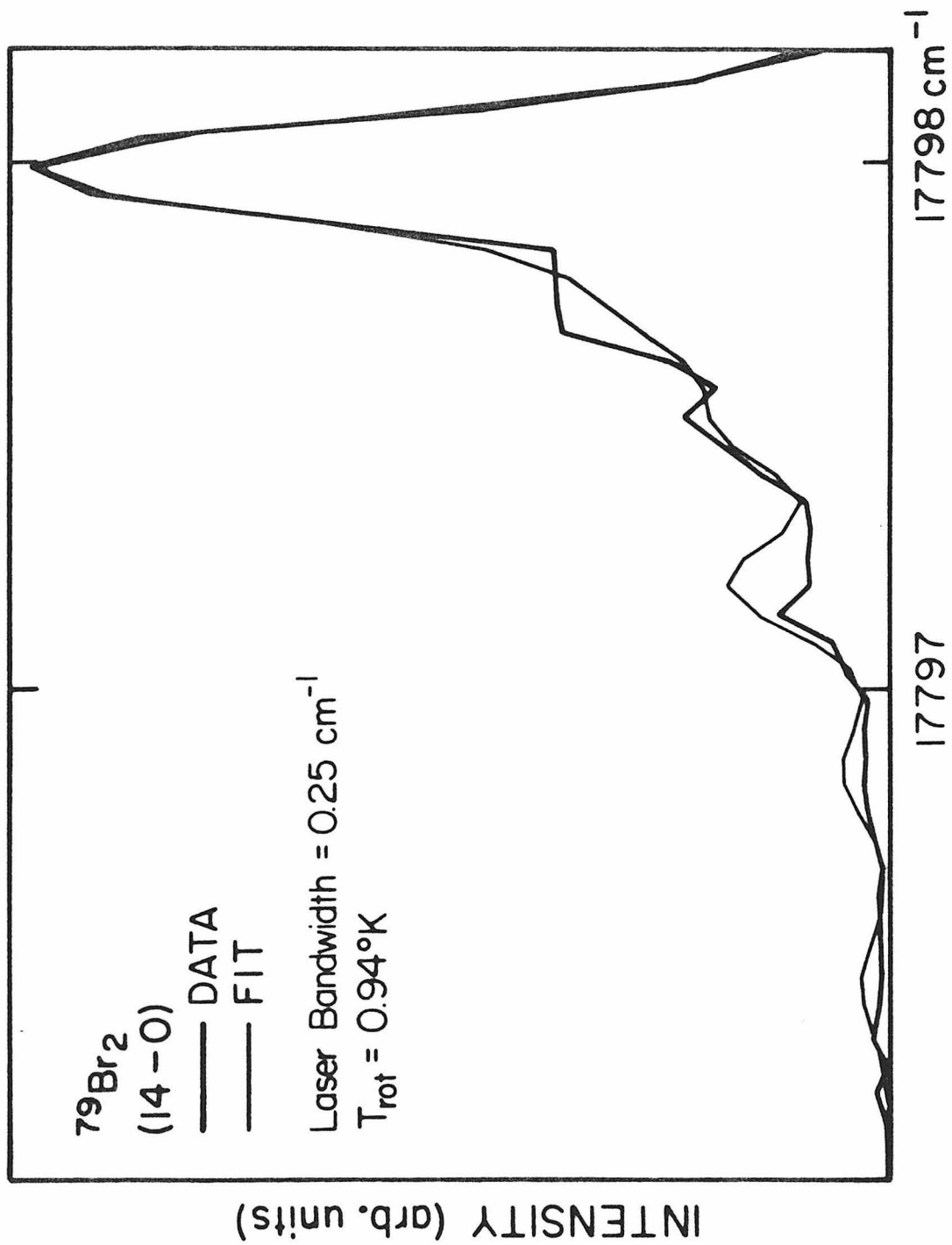
**Figure 6.** The spectral shift of van der Waals band origins relative to the associated Br<sub>2</sub> band origins as a function of the level of vibronic excitation. The lines are linear least squares fits to all data for each complex containing a specified number of Ne atoms.



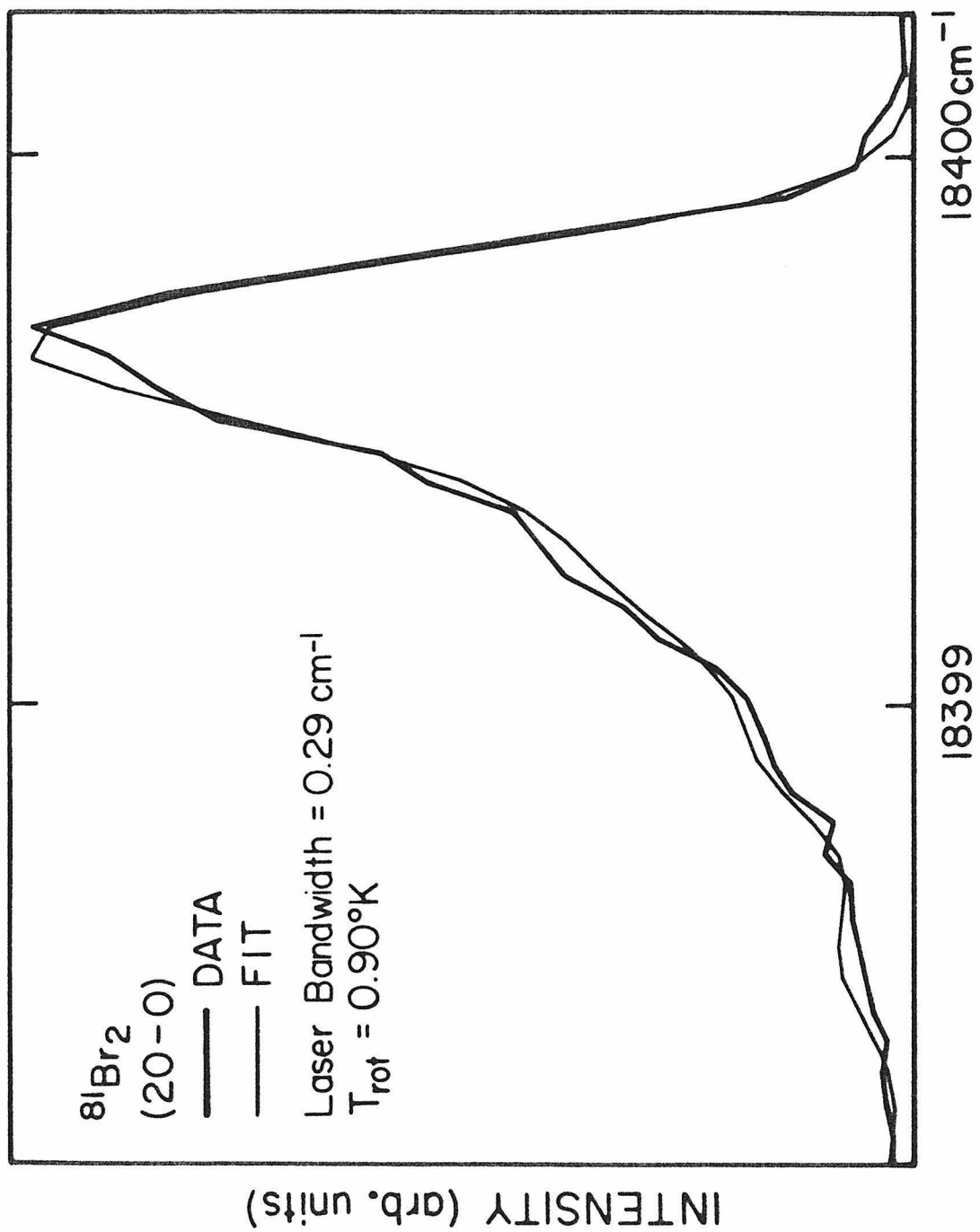
a convenient empirical verification of the manufacturer-specified laser bandwidth versus wavelength as well as deducing the rotational temperature of the beam. Spin degeneracy was, of course, taken into account and nuclear spin states were assumed to be unequilibrated. The natural linewidth of Br<sub>2</sub> rotational lines was neglected since the nuclear hyperfine splitting is only a few hundred megahertz<sup>40</sup> compared with a typical laser bandwidth of 0.30 cm<sup>-1</sup>. Figures 7-9 display the experimental and best fit calculated spectra for Br<sub>2</sub> vibronic bands (14-0), (20-0), and (30-0). They illustrate the quality of the fits which were obtained and show that the laser bandwidth largely determines the overall appearances of the bands. The rotational temperature of the jet cooled Br<sub>2</sub> was found to be 0.95°K and nearly all fits to the data yielded values within ±0.05° of this temperature when the stagnation pressure was held at its maximum of 260 psi. Also, the values for the laser bandwidth computed from the spectra were in very good agreement with those specified for the laser.

Figure 10 shows a signal averaged spectrum of the Ne<sup>79</sup>Br<sup>81</sup>Br band associated with the (14-0) band of Br<sub>2</sub>. Figure 11 displays the analogous spectrum corresponding to the (21-0) band. Comparing the two bands, one may easily see that the spectrum, on further excitation from v' = 14 to v' = 21, becomes both broader and more symmetric. This trend continues to higher v' as may be seen in Figure 12, which shows the fluorescence excitation spectrum of the (29-0) band of Br<sub>2</sub> with associated van der Waals complex bands. The NeBr<sub>2</sub> bands at this v' are now several wavenumbers in width and, except for the Ne<sup>79</sup>Br<sub>2</sub> band, are badly overlapped by the other isotopic Br<sub>2</sub> bands. Spectra such as this at high v' posed the additional

**Figure 7.** Computer fit to the excitation spectrum of the (14-0) vibronic band of  $^{79}\text{Br}_2$ . The same expansion conditions as tabulated in Figure 5 were used in obtaining the experimental spectrum.



**Figure 8.** Computer fit to the experimental excitation spectrum of the (20-0) vibronic band of  $^{81}\text{Br}_2$ . The experimental conditions are the same as those given for the spectra in Figure 2.



**Figure 9.** Computer fit to the fluorescence excitation spectrum of the (30-0) vibronic band of  $^{79}\text{Br}_2$ . Identical experimental conditions were used in obtaining this data as were used in Figure 2.

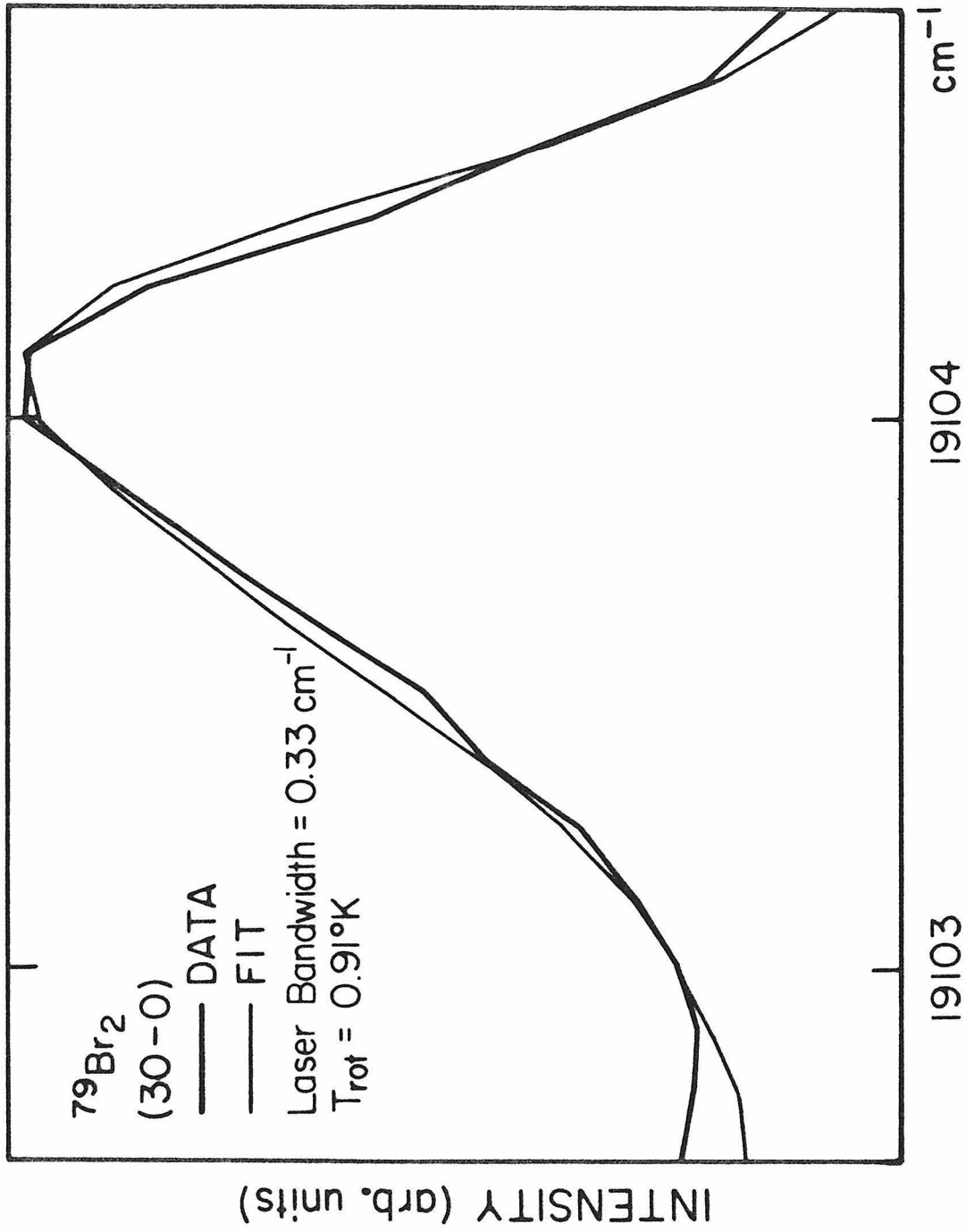


**Figure 10.** Fluorescence excitation spectrum of the (14-0) vibronic band of  $\text{Ne}^{79}\text{Br}^{81}\text{Br}$ . A Schott OG 590 color filter was used. This is a signal averaged spectrum with  $\sim 10$  times the signal as the single scan of Figure 5.

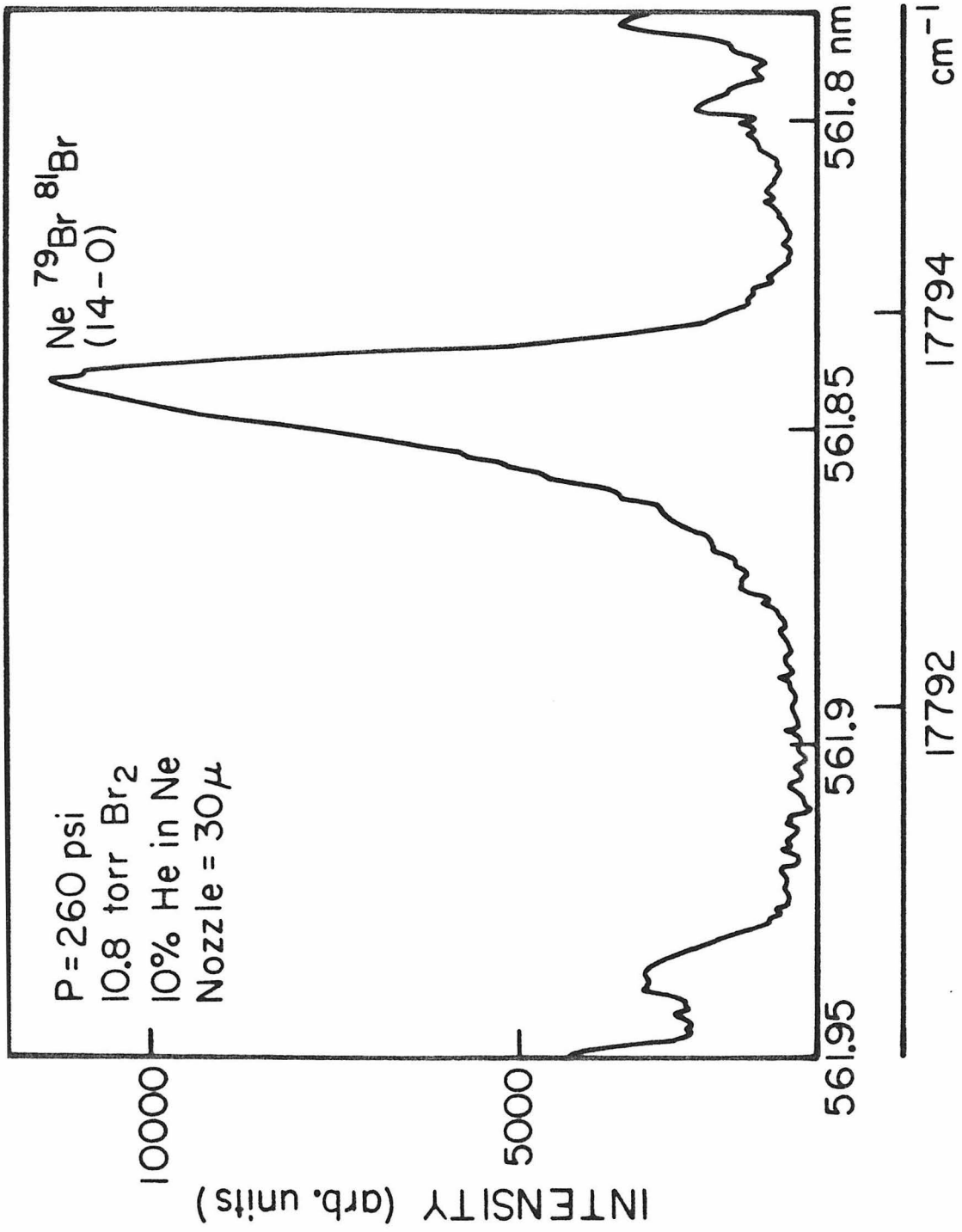


**Figure 11.** Fluorescence excitation spectrum of the (21-0) vibronic band of  $\text{Ne}^{79}\text{Br}^{81}\text{Br}$ . A schott OG 570 color filter was used. This signal averaged spectrum is the superposition of 10 scans over the appropriate wavelengths of the spectrum in Figure 2.

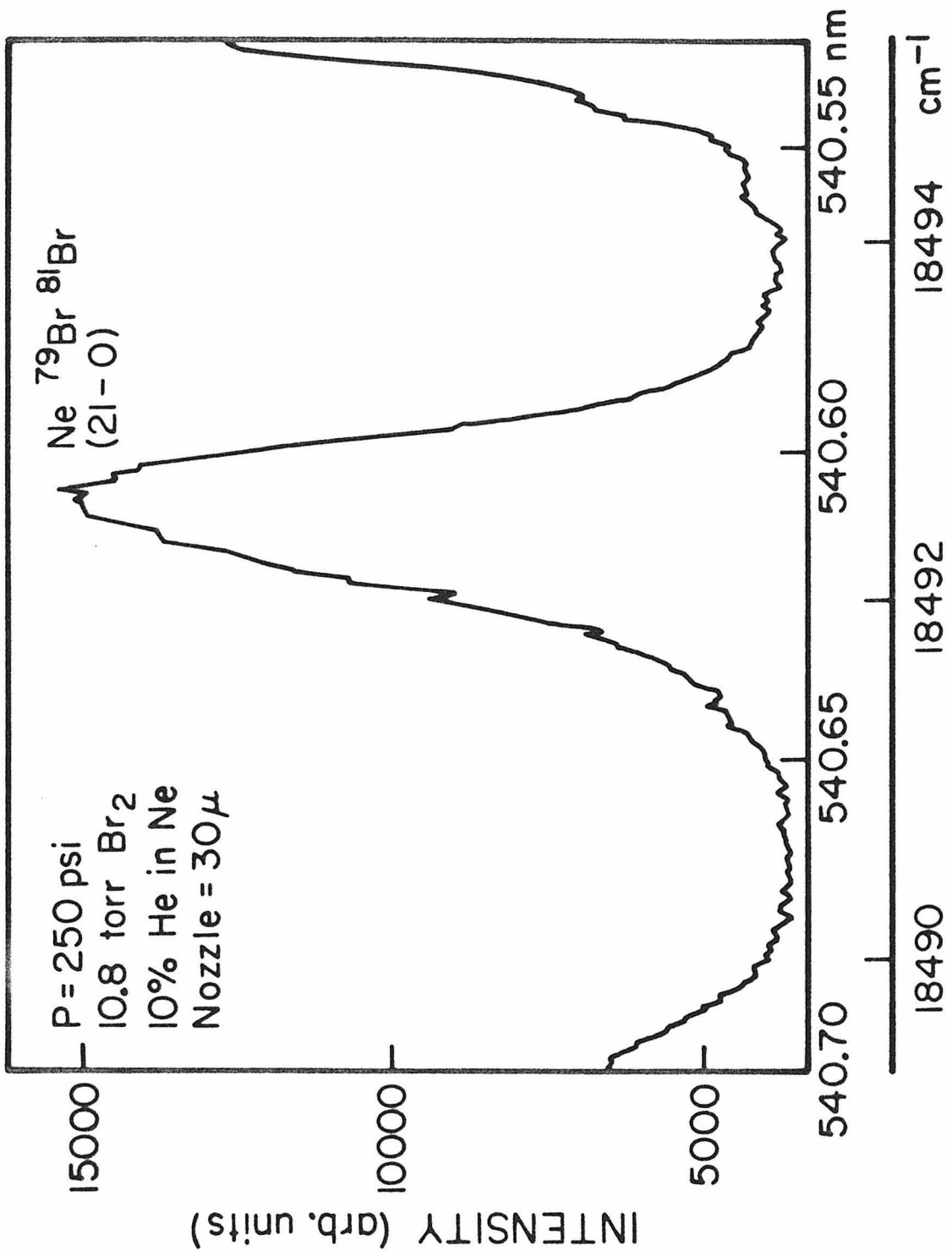
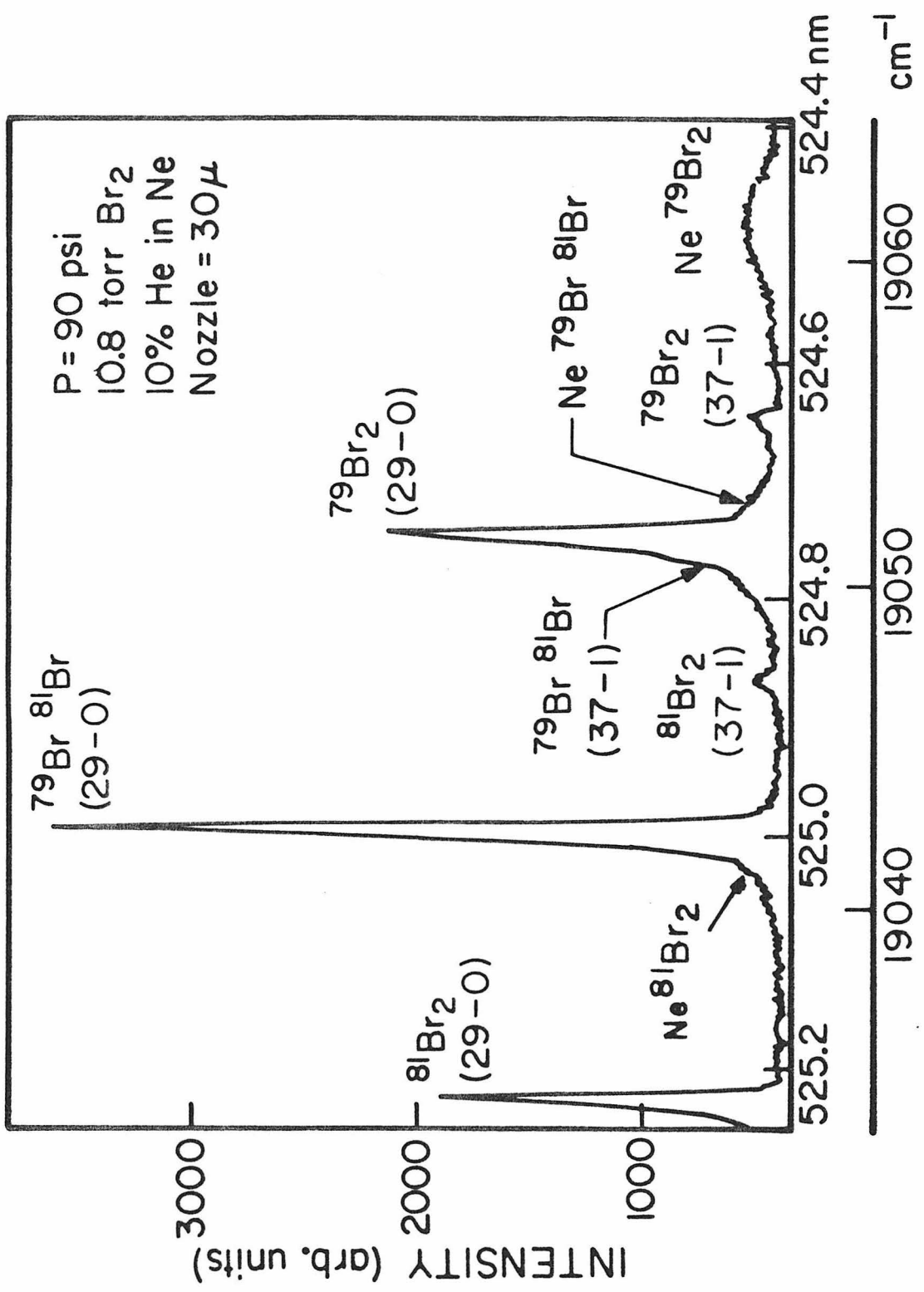


**Figure 12.** Fluorescence excitation spectrum of the (29-0) vibronic band of Br<sub>2</sub> and associated van der Waals bands. A Schott OG 570 color filter was used.



problem of overlapping  $\text{Ne}_2^{79}\text{Br}^{81}\text{Br}$  and  $\text{Ne}^{79}\text{Br}_2$  bands. However, this type of contamination of  $\text{Ne}^{79}\text{Br}_2$  features was eliminated by reducing the nozzle pressure to discriminate against the formation of complexes containing more than one Ne atom. This, of course, resulted in a slightly higher rotational temperature in molecules in these weaker expansions and this was taken into account in the analysis of the bands taken under these conditions.

Clearly, there is evidence of lifetime broadening in  $\text{NeBr}_2$  excited to higher vibrational levels of the  $\text{Br}_2 \text{B}^3\Pi_{0_u^+}$  electronic state. In order to ascertain to what extent vibrational excitation results in a decrease in the lifetime of  $\text{NeBr}_2$ , it was necessary to deconvolve the laser bandwidth from the spectra as well as to interpret the rotational structure of  $\text{NeBr}_2$  bands.

Since individual rotational lines of  $\text{NeBr}_2$  were not resolvable, very little structural information could be gleaned from the spectra. However, the molecules  $\text{NeCl}_2$ <sup>41</sup> and  $\text{HeI}_2$ <sup>23</sup> have been shown rather conclusively to have T-shaped equilibrium structures. In addition it has been found that the halogen atom separations in these molecules are at most only slightly altered from what they are in corresponding states of the free diatomic molecules. Therefore, for the purpose of band shape analysis,  $\text{NeBr}_2$  was assumed to be "T" shaped with a bromine-bromine distance identical to that in  $\text{Br}_2$ . The additional assumption that the neon-bromine atomic separation in  $\text{NeBr}_2$  be fixed at  $3.58 \text{ \AA}$ , which is the equilibrium binding distance for  $\text{NeKr}$  determined from scattering experiments,<sup>42</sup> was necessary to complete the structure. Justification for this assumption is found in the results of Brinza *et. al.*,<sup>41</sup> where spectra of  $\text{NeCl}_2$  were found to be consistent with the assumption that the neon-chlorine atomic distance in this molecule is nearly

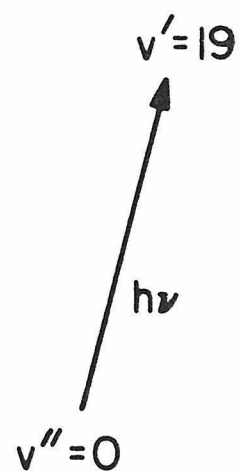
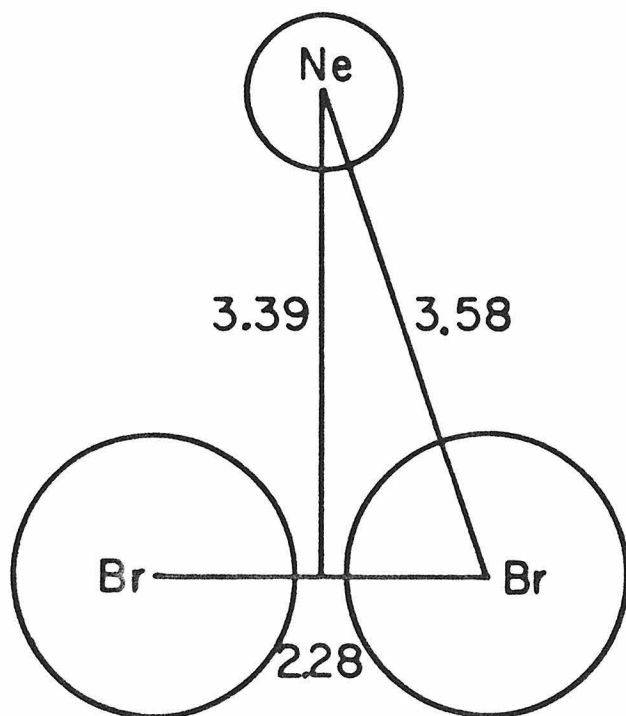
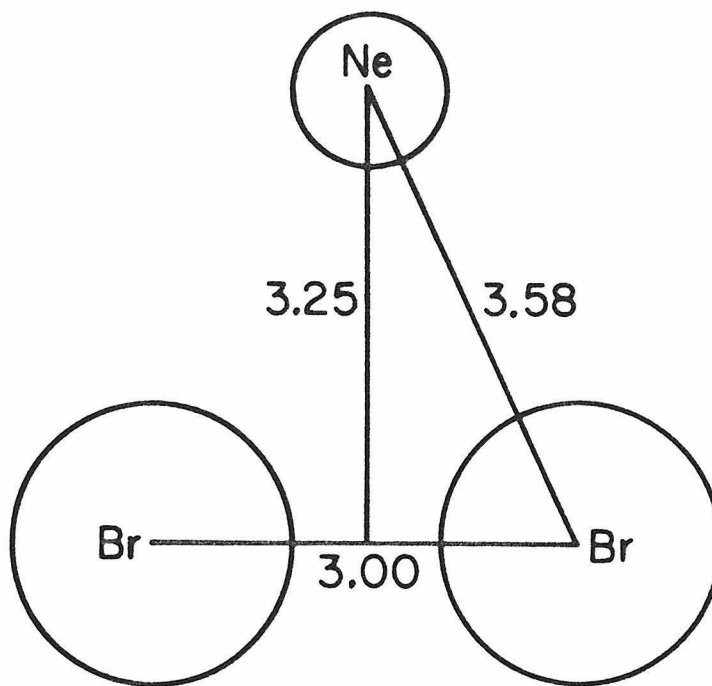
that seen for NeAr.<sup>42</sup> This assumed structure is diagrammed in Figure 13 for a sample transition between the  $v'' = 0$  and  $v' = 19$  vibronic levels.

An asymmetric rotor spectrum calculating program which included convolution of the excitation bandwidth and natural linewidth of the molecular states was used to calculate NeBr<sub>2</sub> band spectra. Rotational constants calculated from the assumed geometrical structure for NeBr<sub>2</sub> were input to the program along with values for the rotational temperature and laser bandwidth which were determined from the fits to the corresponding Br<sub>2</sub> bands measured under identical expansion conditions. The non-linear least squares fitting routine then varied the natural linewidth of the transition along with the band origin frequency to fit the observed spectra. The neon-bromine atomic separation was also varied for several of the bands. Although the fits were largely insensitive to this parameter, no inconsistencies between the experimental band shapes and the assumed NeBr<sub>2</sub> structures were evident.

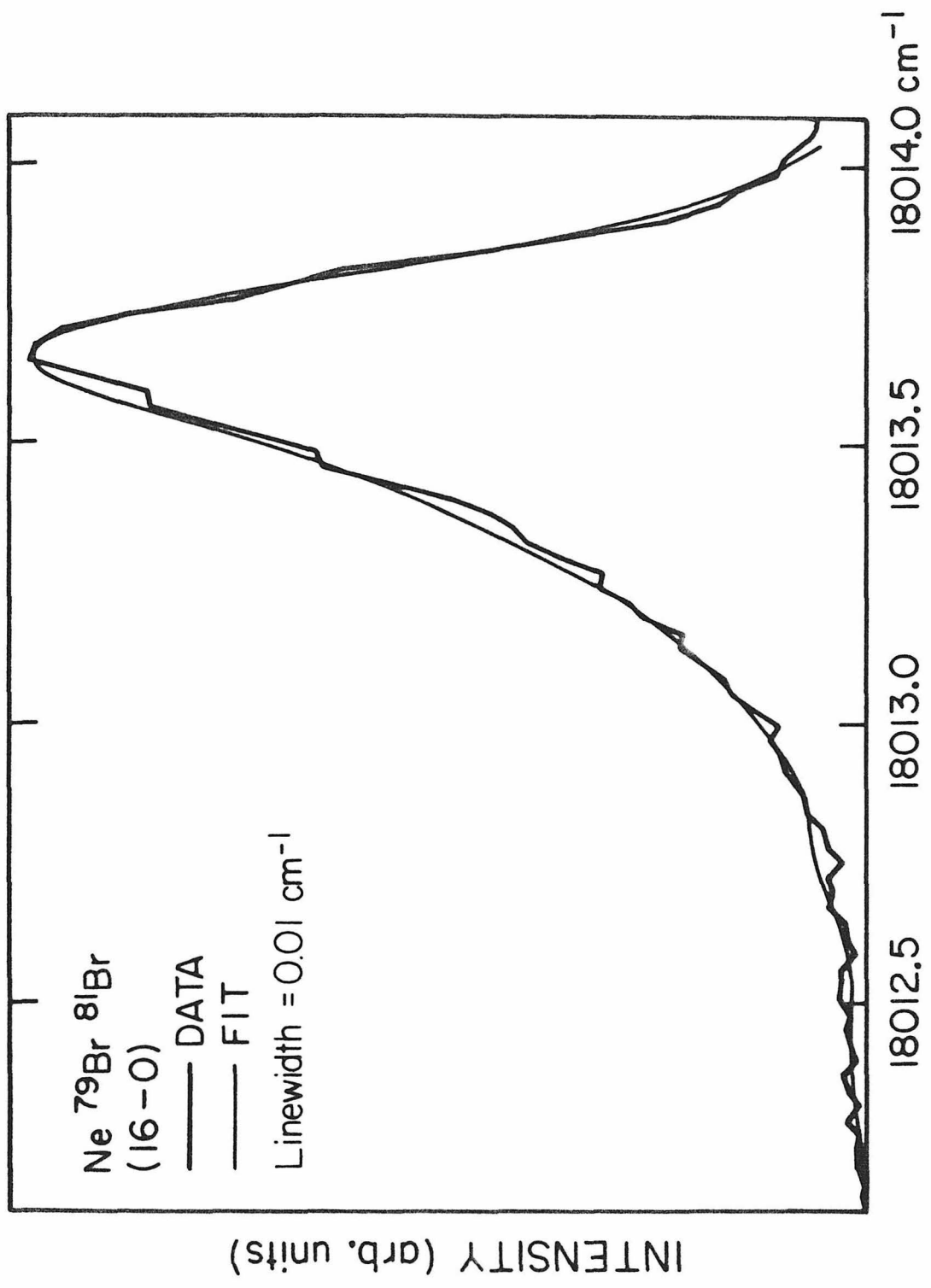
Examples of fits to NeBr<sub>2</sub> bands are displayed in Figures 14-16. The linewidths determined from all fits to NeBr<sub>2</sub> bandshapes are included in Table II. These linewidths are displayed as a function of  $v'$  in Figures 17 and 18. Here it can be seen that the linewidths become undetermined at low  $v'$  levels where it cannot be expected that the fits produce reliable values for linewidths less than  $\sim 1/3$  of the excitation laser bandwidth. The NeBr<sub>2</sub> natural linewidths are shown to generally increase as a function of  $v'$  from  $v' = 16$  to  $v' = 27$  or 28 beyond which the linewidths decrease.

Figure 19 shows a signal averaged spectrum of van der Waals complex bands where the number of Ne atoms bound in the complexes varies from 1-3.

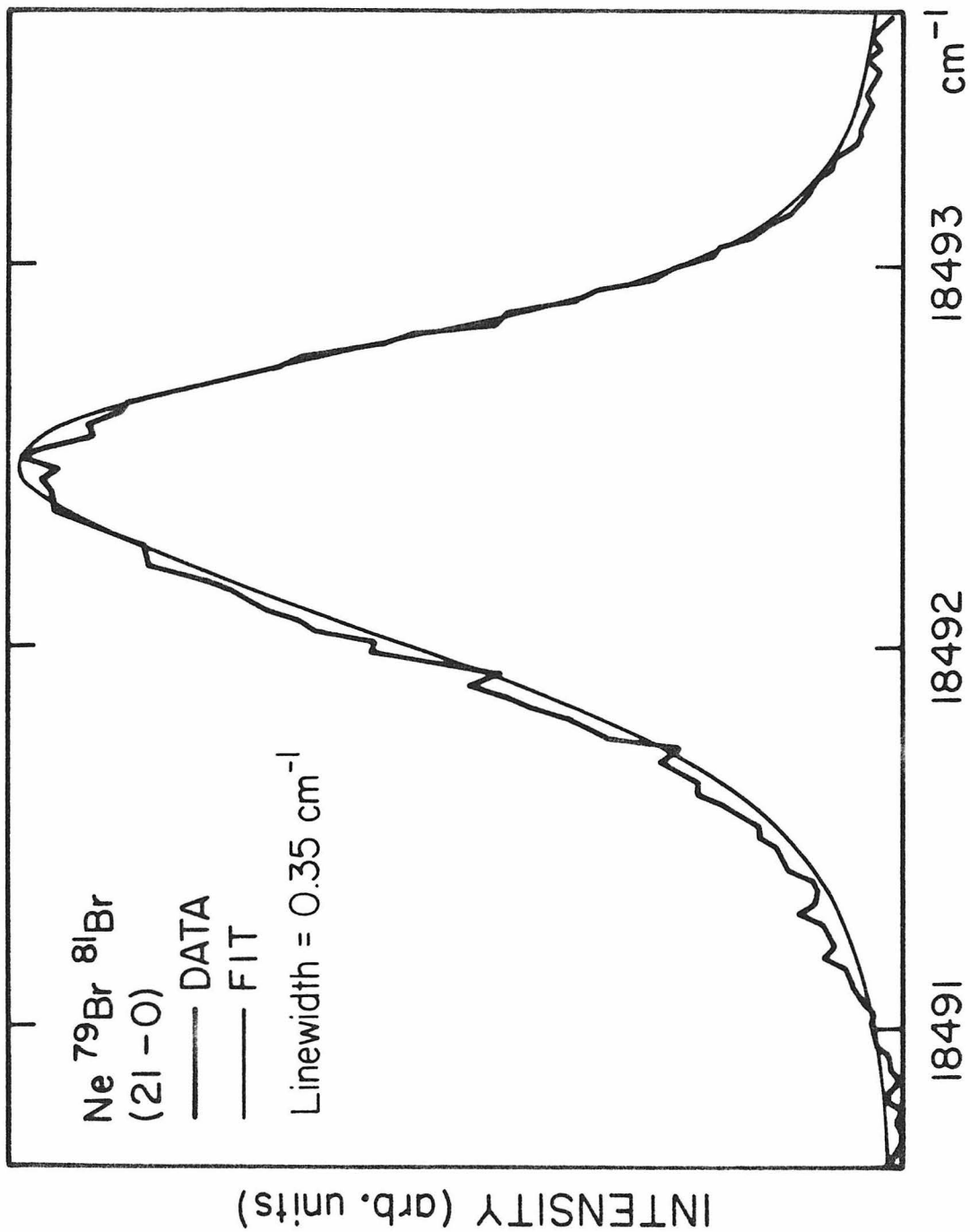
**Figure 13.** Example structures used to calculate rotational constants for the computer fitting of NeBr<sub>2</sub> vibronic bands. Bond distances are in angstroms.



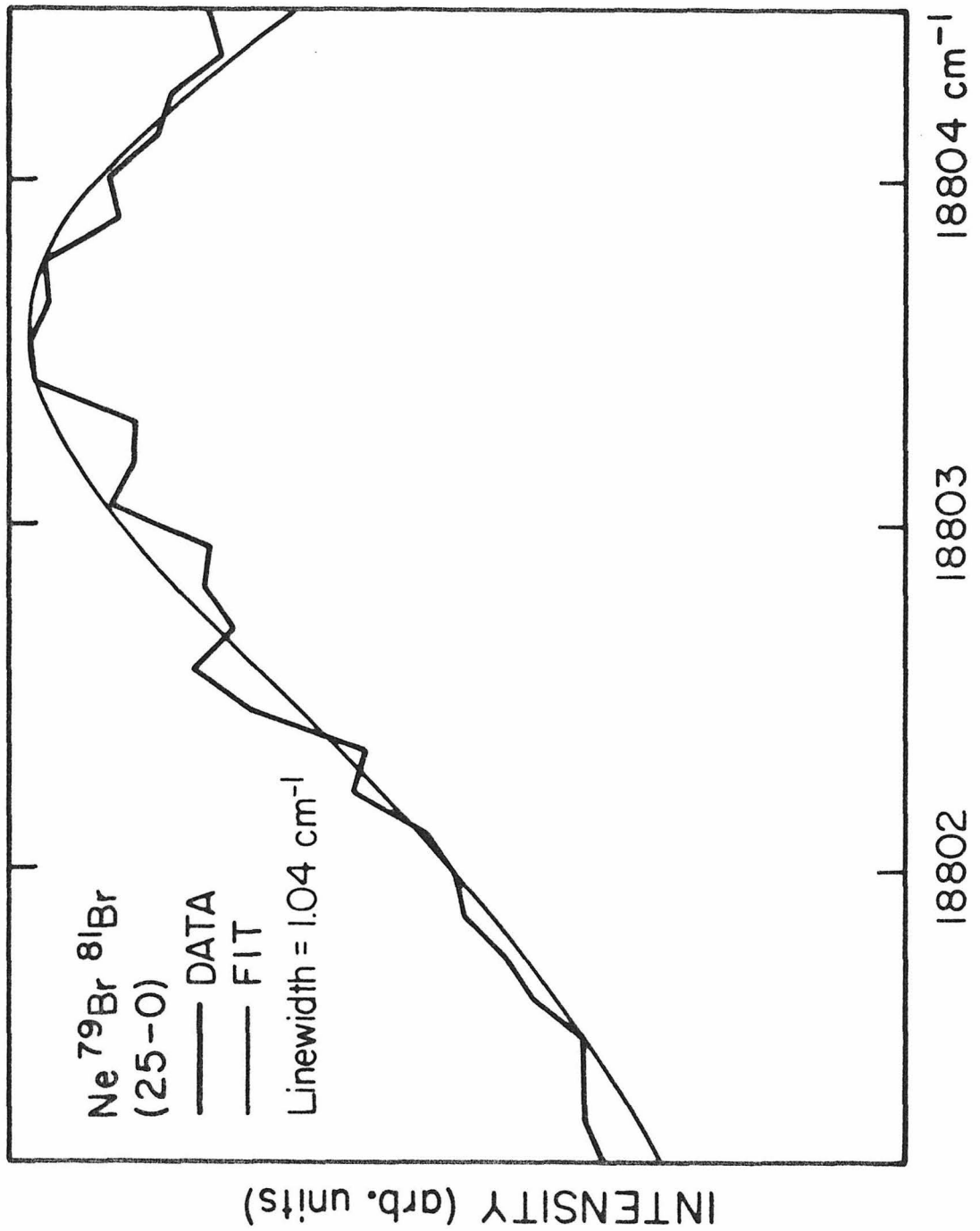
**Figure 14.** Computer fit to the Ne<sup>79</sup>Br<sup>81</sup>Br (16-0) vibronic band shape. The laser bandwidth was 0.27 cm<sup>-1</sup>.



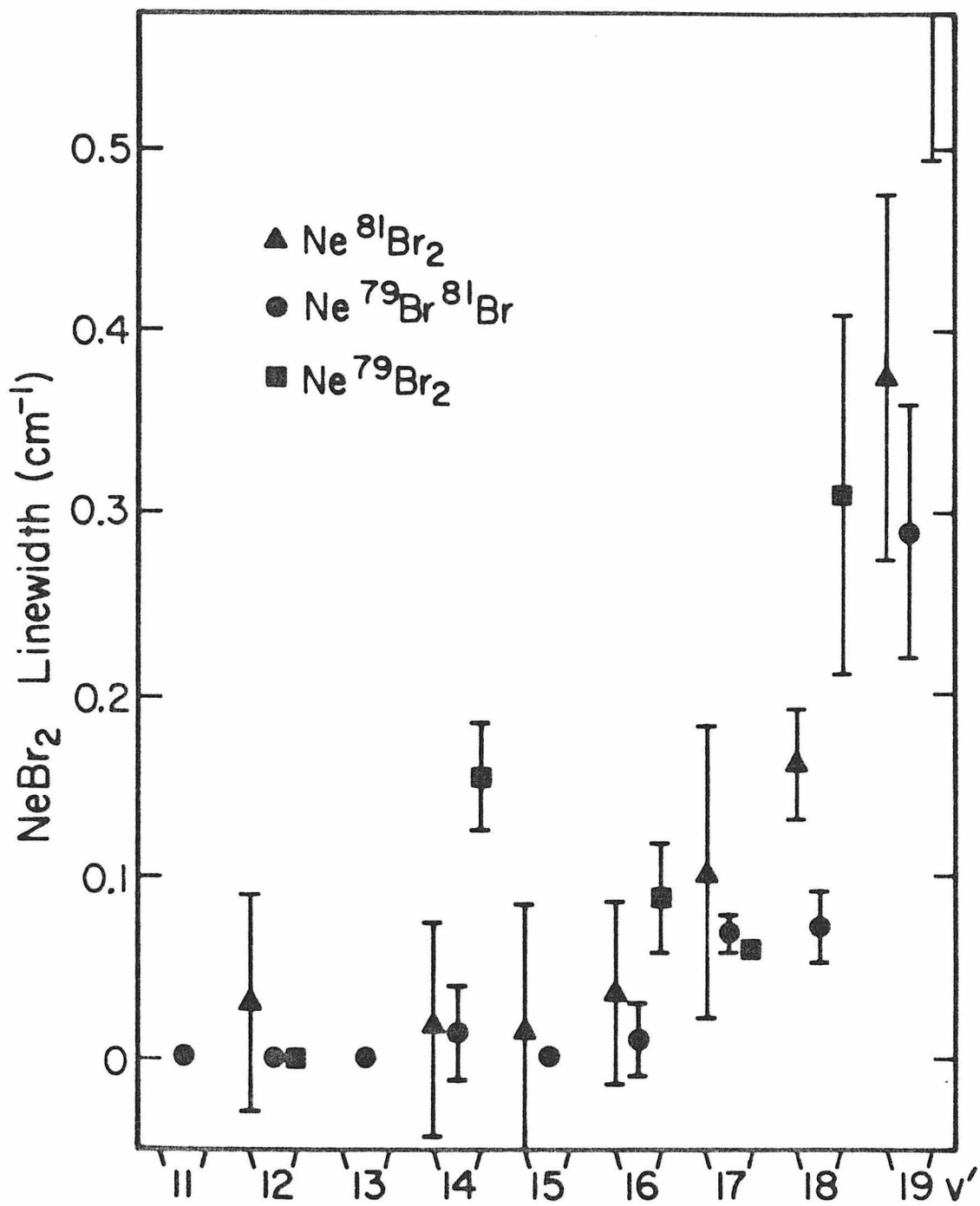
**Figure 15.** Computer fit to the  $\text{Ne}^{79}\text{Br}^{81}\text{Br}$  (21-0) vibronic bandshape. The laser bandwidth was  $0.30 \text{ cm}^{-1}$ .



**Figure 16.** Computer fit to the Ne<sup>79</sup>Br<sup>81</sup>Br (25-0) vibronic bandshape. The laser linewidth was 0.31 cm<sup>-1</sup>.



**Figures 17 and 18.** Natural linewidths of NeBr<sub>2</sub> bands determined from computer fits to the bandshapes as a function of the level of vibronic excitation. The error bars are intended only to give an idea of the relative accuracy of data points and are not to be taken as absolute standard deviations. Data points at low  $v'$  for which no error bars are shown in fact have extremely large uncertainties.



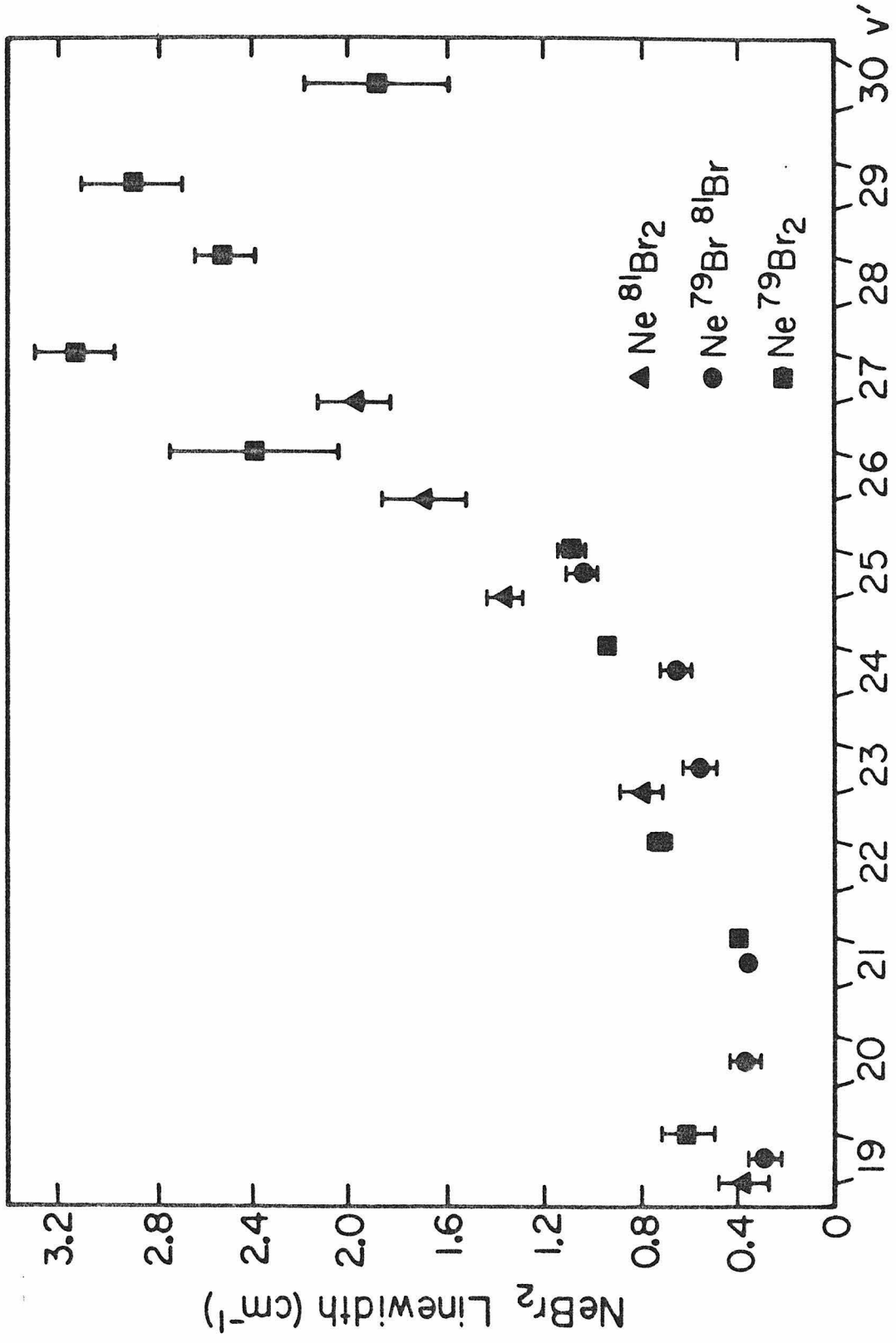
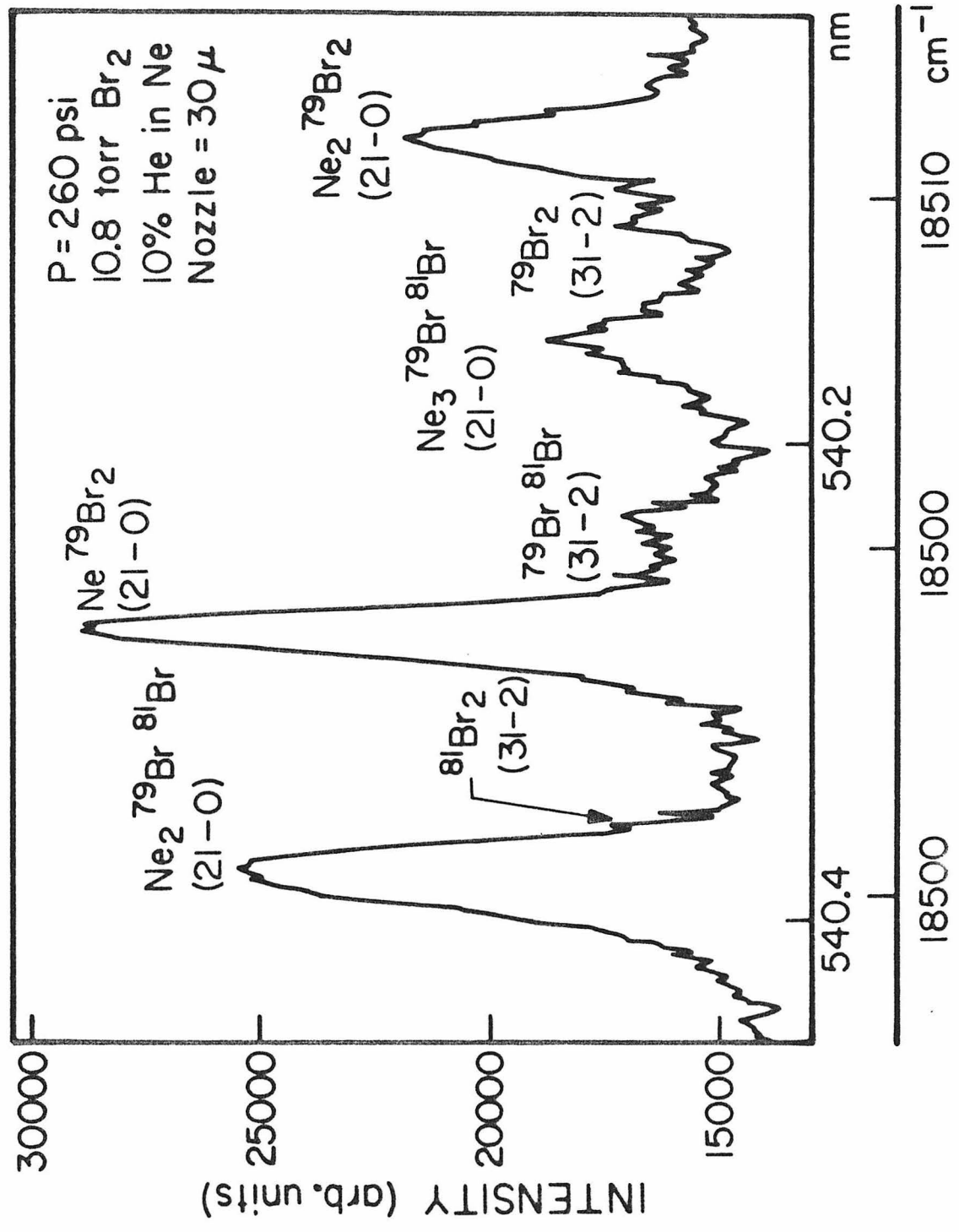


**Figure 19.** Signal averaged fluorescence excitation spectrum of a portion of the scan in Figure 3 showing (12-0) bands of van der Waals complexes containing 1-3 Ne atoms.



It can be clearly seen that the width of these features increases with the number of Ne atoms in the complex. No attempt was made to fit band shapes for complexes containing more than one neon atom. Thus, it is difficult to determine whether the increased width for these complexes is due to shorter lifetimes or simply broader rotational structure. Bands of Br<sub>2</sub> and NeBr<sub>2</sub>, however, form a head in their R branches at very low J.<sup>43</sup> Therefore, upper limits to the linewidths of Ne<sub>n</sub>Br<sub>2</sub> bands for n = 2-3 were estimated by measuring the half-widths of the bands to the blue side of the observed features. These estimated upper limits to the linewidths of larger complexes of Ne and Br<sub>2</sub> are included in Table II.

**Table II.** Natural linewidths of van der Waals bands in cm<sup>-1</sup>. NeBr<sub>2</sub> linewidths are determined from computer fits to the data. Widths for all other complexes are upper limits estimated from the half widths of R branch heads. Error limits are only indicative of the ability of the fits to determine the linewidth and should not be taken as standard errors.

v'	Ne <sup>81</sup> Br <sub>2</sub>	Ne <sup>79</sup> Br <sub>2</sub>	Ne <sup>79</sup> Br <sup>81</sup> Br	Ne <sub>2</sub> Br <sub>2</sub>
11	--	--	0.002	--
12	0.03 ± 0.06	0.001 --	0.001	--
13	0.001	--	--	--
14	0.018 ± 0.06	0.155 ± 0.03	0.014 ± 0.026	--
15	0.015 ± 0.07	--	0.001	--
16	0.036 ± 0.05	0.089 ± 0.03	0.011 ± 0.02	--
17	0.102 ± 0.08	0.06	0.070 ± 0.01	--
18	0.162 ± 0.03	0.309 ± 0.01	0.072 ± 0.02	--

Table II. Continued.

$\nu'$	Ne <sup>81</sup> Br <sub>2</sub>	Ne <sup>79</sup> Br <sub>2</sub>	Ne <sup>79</sup> Br <sup>81</sup> Br	Ne <sub>2</sub> Br <sub>2</sub>	Ne <sub>3</sub> Br <sub>2</sub>
19	0.376 ± 0.10	0.614 ± 0.12	0.290 ± 0.97	--	--
20	--	--	0.376 ± 0.06	--	--
21	--	0.400 ± 0.02	0.346 ± 0.03	1.1,0.9	1.3
22	--	0.738 ± 0.04	--	--	--
23	0.800 ± 0.09	--	0.561 ± 0.07	--	--
24	--	0.937 ± 0.04	0.655 ± 0.06	--	--
25	1.36 ± 0.07	1.09 ± 0.05	1.04 ± 0.06	--	--
26	1.69 ± 0.17	2.38 ± 0.35	--	--	--
27	1.97 ± 0.15	3.12 ± 0.16	--	3.2	--
28	--	2.50 ± 0.12	--	2.7	--
29	--	2.88 ± 0.20	--	3.2	--
30	--	1.88 ± 0.29	--	3.9	--

Finally, it should be noted, that in determining the spectral shifts of NeBr<sub>2</sub> bands from their associated Br<sub>2</sub> bands, the origins determined from the fits to their bandshapes were used and this is how the data in Table I and Figure 6 were obtained. For the case of larger complexes, however, the band origins were assumed to coincide with the peak of the band profile and the shifts of these points from the corresponding Br<sub>2</sub> origins are reported.

## Discussion

The spectral shifts of  $\text{Ne}_n\text{Br}_2$  bands relative to the parent  $\text{Br}_2$  band origins provide information about the binding in these complexes. First, the complex bands are always observed at higher frequencies than the  $\text{Br}_2$  vibronic bands. This implies that the van der Waals well depth in the excited electronic state is less than in the ground state. Secondly, since the shifts increase with excitation to higher vibrational levels of the excited electronic state, it can be deduced that the dissociation energy of these complexes decreases with increasing vibrational energy content in the  $\text{Br}_2$  bond. This effect is small, however, indicating a change in binding energy of only a couple of wavenumbers for  $\text{NeBr}_2$  over the range of vibrational levels  $v' = 11 - 30$ . Thus, it may be concluded that the  $\text{Ne-Br}_2$  bond has only a very small effect on the electronic structure of  $\text{Br}_2$  in either the ground  $X^1\Sigma_{\text{og}}^+$  or excited  $B^3\Pi_{\text{ou}}^+$  state. This is very similar to the results obtained for complexes containing  $\text{I}_2^{21,24,27}$  and  $\text{Cl}_2^{29,41}$  and is also consistent with the structure assumed here for  $\text{NeBr}_2$ .

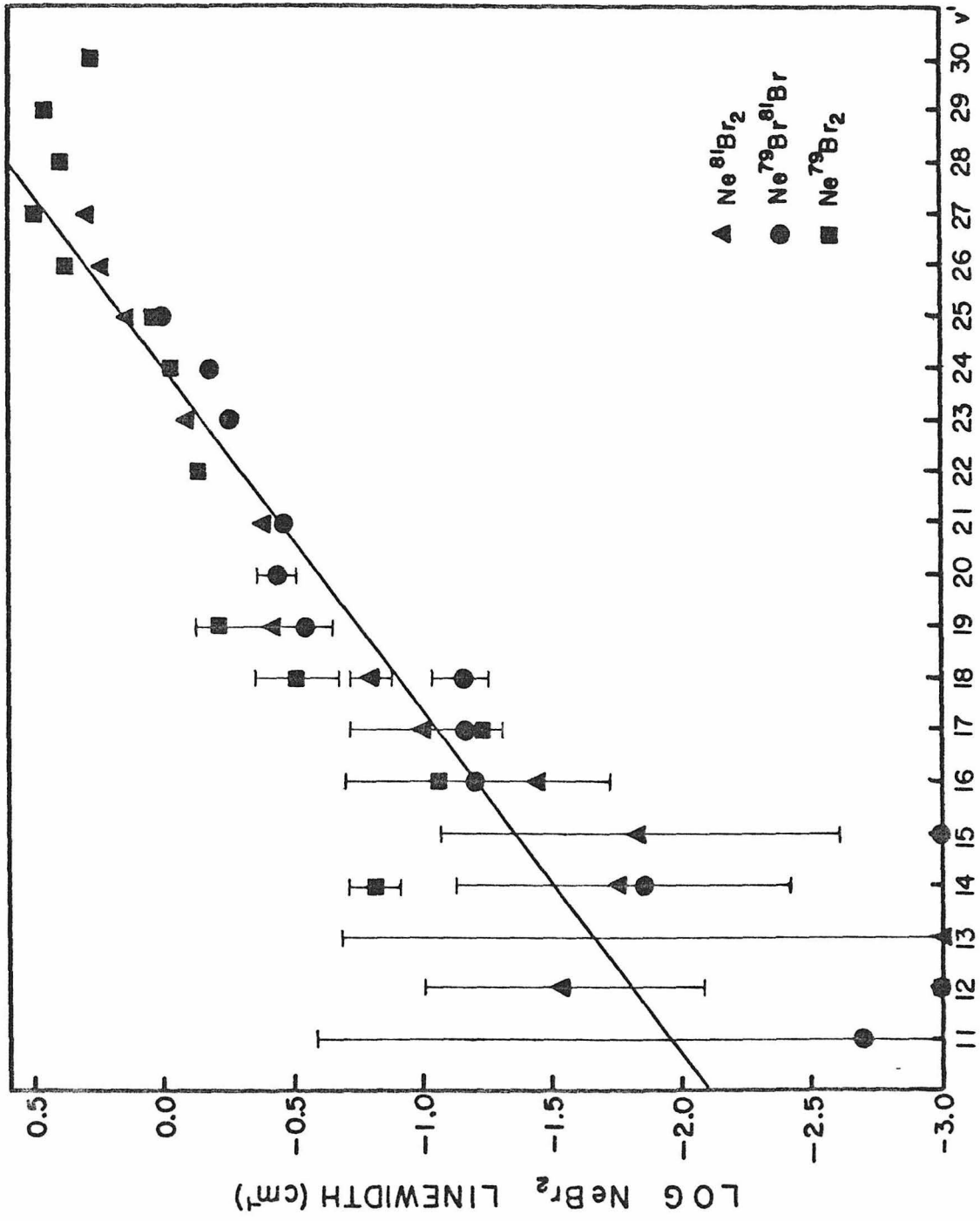
The additive nature of the shifts for increasing numbers of Ne atoms bound in the complexes provides some insight into the structures of these van der Waals molecules. It indicates that successive Ne atoms are bound in roughly equivalent positions around the  $\text{Br}_2$  molecule. Levy and co-workers have forwarded two alternative structures to account for this constant nature of the shifts for  $\text{Ne}_n\text{I}_2$  molecules with  $n = 1 - 6$ .<sup>27</sup> (The shift for  $\text{Ne}_7\text{I}_2$  was found to be inconsistent with the assumption that the seventh neon atom occupied a position equivalent to that of the first six.) They suggest either a belt model where all Ne atoms occupy equivalent equatorial positions about

the halogen-halogen bond or an ethane-like structure. The former configuration is preferred here in light of the T-shaped structures indicated for  $\text{HeI}_2$ <sup>23</sup> and  $\text{NeCl}_2$ <sup>41</sup> and the fact that the  $\text{NeBr}_2$  band shapes reported here are also found to be consistent with a T-shaped equilibrium structure.

The linewidths of vibronically excited  $\text{NeBr}_2$ , which are graphed in Figures 17 and 18 as a function of  $v'$ , have been replotted on a log scale in Figure 20. Since the crossing of the dissociative  $^1\Pi_{1u}$  state with the  $B^3\Pi_{0u}^+$  state of  $\text{Br}_2$  occurs at  $v' = \sim 3$ ,<sup>44</sup> these linewidths for bands with  $v' = 11-30$  are considered to be determined by vibrational rather than electronic predissociation. Furthermore, electronic predissociation would result in non-fluorescent Br atoms as products, and thus a decrease in signal would be observed as the rate of this process were to increase. No decrease in signal with increasing linewidth was observed.

The line in Figure 20 is a linear least squares fit to the data points corresponding to  $v' = 16$  through  $v' = 27$  with equal weights given to all data points used in the fit. The linewidths for vibronic bands with  $v' < 16$  were not included, because they are not believed to be reliable due to the fact that the widths at these  $v'$  are much less than the exciting laser bandwidth as may be seen from Figure 17. The linewidths for  $v' > 27$  will be discussed presently. The slope of the line in Figure 20 is  $0.15 \log \text{cm}^{-1}/v'$ . This is a far weaker dependence on  $v'$  of the rate of vibrational predissociation than was determined both experimentally<sup>25</sup> and theoretically<sup>45</sup> for  $\text{HeI}_2$ , where an approximately quadratic behavior was observed. However, it has been pointed out that the calculated predissociation rates depend to a large extent on the details of the particular

**Figure 20.** Semi-log plot of the data displayed in linear fashion in Figures 17 and 18. The line is a linear least squares fit to the data points corresponding to  $v' = 16$  through  $v' = 27$ .



model potential chosen.<sup>33,46</sup> Thus, explanation of this weak dependence on  $v'$  must await detailed calculations for the specific case of NeBr<sub>2</sub>.

The predissociation lifetimes of NeBr<sub>2</sub> calculated from the measured linewidths using the relation

$$\tau = (2\pi W (\text{FWHM}))^{-1},$$

where  $W$ , the linewidth, is in Hz, range from 84 psec for  $v' = 16$  to 1.7 psec for  $v' = 27$ . Extrapolating the line in Figure 20 to  $v' = 1$ , a predissociation lifetime of 15 nsec is predicted for NeBr<sub>2</sub> with one quantum of vibrational energy initially localized in the Br<sub>2</sub> bond.

In spite of concerted efforts to observe van der Waals complex bands associated with vibronic bands of Br<sub>2</sub> originating from the  $v'' = 1$  level (which had appreciable intensity as may be seen in Figs. 2 and 5), no such features were detected. It is estimated that if bands corresponding to vibrationally "hot" NeBr<sub>2</sub> were present, their intensity must be at least 10,000 times less than the corresponding Br<sub>2</sub> vibronic bands. It is therefore assumed that NeBr<sub>2</sub> in the  $v'' = 1$  level of the Br<sub>2</sub> X<sup>1</sup>Σ<sub>g</sub><sup>+</sup> state predissociates before reaching the intersection of the exciting laser and the molecular beam. This places an upper limit to the predissociation lifetime of NeBr<sub>2</sub> in the  $v'' = 1$  vibrational level of 10 μsec, determined by the time-of-flight from the nozzle to the laser interaction region.

In light of Ewing's momentum gap theory<sup>36</sup> and Beswick and Jortner's energy gap law<sup>33</sup> one would predict that the rate of predissociation would reach a maximum when the energy of the vibrational quanta of the

chemically bound portion of the complex was resonant with the dissociation energy of the van der Waals bond. Since diatomic halogen molecules have a finite anharmonicity, excitation to successively higher vibronic states, where the vibrational quanta become smaller, should eventually reach this resonance. Further excitation should result in the closing of the single quantum predissociation channel and the opening of a two quantum channel. This effect is believed to be responsible for the decrease in linewidths for NeBr<sub>2</sub> vibronic bands with  $v' > 27$  which is clearly seen in Figure 18. The known vibrational level spacing in Br<sub>2</sub> between states  $v' = 27$  and  $v' = 26$  is thus an estimate of the van der Waals bond dissociation energy in electronically excited NeBr<sub>2</sub>. This value is  $64 \pm 4 \text{ cm}^{-1}$  where the anharmonicity of  $B^3\Pi_{0_u^+} \text{ Br}_2^{38}$  is chosen as the estimated error. Subsequently, by adding the spectral shift of  $\sim 9 \text{ cm}^{-1}$  to this upper state D<sub>0</sub>, an estimate of  $73 \text{ cm}^{-1}$  is obtained for the dissociation energy of ground electronic state NeBr<sub>2</sub>. Sharfin *et. al.*<sup>46</sup> have observed this same effect in higher ( $v' = 57$ ) vibronic bands of HeI<sub>2</sub> while Beswick and co-workers<sup>47</sup> have performed detailed calculations on this molecule which qualitatively predict this behavior.

Although the theoretical approaches have achieved significant success in predicting the qualitative nature of vibrational predissociation in van der Waals molecules, they have been struggling to reach absolute agreements. The theories have advanced some simple approximate expressions for these predissociation lifetimes. Ewing<sup>36</sup> has correlated the predissociation lifetimes from detailed calculations on numerous van der Waals molecules with the dimensionless parameter

$$DP = \frac{(2\mu_v(W_{AB}-D_0))^{1/2}}{\alpha\hbar}$$

where  $\alpha$  is the range parameter of the Morse potential used to describe the van der Waals bond. He found the relation

$$\log \tau = 0.75 DP - 11.8$$

to approximately hold for over 20 orders of magnitude in  $\tau$ . Values of DP were computed here for several states of NeBr<sub>2</sub>. The experimental values for  $D_0$  and the vibrational level spacings,  $W_{AB}$ , determined from the Br<sub>2</sub> absorption measurements of Coxon and coworkers<sup>37,38</sup> were used. A value of  $1.4 \cdot 10^8 \text{ cm}^{-1}$  was assumed for  $\alpha$  which is the range parameter determined for NeI<sub>2</sub> from the frequency of the van der Waals stretch in this molecule.<sup>27</sup> The corresponding values of the predissociation lifetime for these DP are listed in table III. The table also includes the experimental values determined in this work as well as predissociation lifetimes calculated from Beswick and Jortner's<sup>33,34</sup> approximate formula for T-shaped van der Waals molecules. This formula utilizes the same input parameters as Ewing's DP but is an actual analytical expression (albeit approximate) for the lifetime assuming that the AB bond is harmonic.

It is seen from table III that the calculated values consistently overestimate the predissociation lifetimes of NeBr<sub>2</sub> except for the  $v' = 27$  level where there is good agreement between the experimental and

**Table III.** Experimental and calculated predissociation lifetimes for NeBr<sub>2</sub>. The "experimental" value for v' = 1 is an interpolation of the data in Figure 20. See text for details of the calculations.

State		Experiment	Calculated	
			Beswick-Jortner Energy Gap	Ewing Momentum Gap
X <sup>1</sup> Σ <sub>g</sub> <sup>+</sup>	v'' = 1	10 μsec	250 μsec	790 μsec
B <sup>3</sup> Π <sub>g</sub> <sup>+</sup>	v' = 1	15 nsec	130 nsec	540 nsec
	v' = 16	84 psec	8 nsec	8 nsec
	v' = 27	1.7 psec	5 nsec	2 psec

momentum gap predissociation lifetimes. The correct trends are predicted, and, as has been already mentioned, the calculated lifetimes are extremely sensitive to the potential parameters which are largely uncertain for NeBr<sub>2</sub>.

This work is therefore seen as a single but significant step in the understanding of the bonding and dynamics of van der Waals molecules.

### References and Notes

- (1) For reviews see: Ewing, G. E. Angew. Chem. Int. Ed. **1972**, 11, 486. Klemperer, W.; Bunsenges, Br. Phys. Chem. **1974**, 78, 128. Ewing, G. E. Accts. Chem. Res. **1975**, 8, 1845. Ewing, G. E. Can. J. Phys. **1976**, 54, 487. Blaney, B. L.; Ewing, G. E. Ann. Rev. Phys. Chem. **1976**, 27, 553.
- (2) Hirschfelder, J. O.; Curtiss, C. F.; Bird, R. B. "Molecular Theory of Gases and Liquids"; Wiley: New York, 1964.
- (3) Casassa, M. P.; Bomse, D. S.; Beauchamp, J. L.; Janda, K. C. J. Chem. Phys. **1980**, 72, 6805.
- (4) Ewing, G. J. Chem. Phys. **1980**, 72, 2096.
- (5) Himes, J. L.; Wiggins, T. A. J. Mol. Spectry. **1971**, 40, 418. Larvor, M.; Hondeau, J.-P.; Haeusler, C. Can. J. Phys. **1978**, 56, 334.
- (6) McKellar, A. R. W.; Welsh, H. L. J. Chem. Phys. **1971**, 55, 595.
- (7) Henderson, G.; Ewing, G. E. Mol. Phys. **1974**, 27, 903.
- (8) Henderson, G.; Ewing, G. E. J. Chem. Phys. **1973**, 59, 2280.
- (9) Long, C. A.; Ewing, G. E. J. Chem. Phys. **1973**, 58, 4824.
- (10) Long, C. A.; Henderson, G.; Ewing, G. E. Chem. Phys. **1973**, 2, 485.
- (11) Smalley, R. E.; Wharton, L.; Levy, D. H. Accts. Chem. Res. **1977**, 10, 139. Levy, D. H.; Wharton, L.; Smalley, R. E. In "Chemical and Biochemical Applications of Lasers", Vol. II; Academic Press: New York, 1977, Chap. 1. Campargue, R. J. Chem. Phys. **1970**, 52, 1795.
- (12) Holmgren, S. C.; Waldman, M.; Klemperer, W. J. Chem. Phys. **1978**, 69, 1661. Novick, S. E.; Janda, K. C.; Holmgren, S. L.; Waldman, M.; Klemperer, W. Ibid. **1976**, 65, 1114. Novick, S. E.; Davies, P.;

- Harris, S. J.; Klemperer, W. Ibid. **1973**, 59, 2273.
- (13) Harris, S. J.; Novick, S. F.; Klemperer. J. Chem. Phys. **1974**, 60, 3208.
- (14) Harris, S. J.; Novick, S. E.; Klemperer, W.; Falconer, W. E. J. Chem. Phys. **1974**, 61, 193.
- (15) Novick, S. E.; Harris, S. J.; Janda, K. C.; Klemperer, W. J. Chem. Phys. **1975**, 63, 881.
- (16) Janda, K. C.; Steed, J. M.; Novick, S. E.; Klemperer, W. J. Chem. Phys. **1977**, 67, 5162.
- (17) Western, C. M.; Langridge-Smith, P. R. R.; Howard, B. J.; Novick, S. E. Mol. Phys. **1981**, 44, 145.
- (18) Casassa, M. P.; Bomse, D. S.; Janda, K. C. J. Chem. Phys. **1981**, 74, 5044.
- (19) Gough, T. E.; Miller, R. E.; Scoles, G. J. Chem. Phys. **1978**, 69, 1588.
- (20) Smalley, R. E.; Auerbach, D. A.; Fitch, P. S. H.; Levy, D. H.; Wharton, L. J. Chem. Phys. **1977**, 66, 3778.
- (21) Smalley, R. E.; Levy, D. H.; Wharton, L. J. Chem. Phys. **1976**, 64, 3266.
- (22) Kim, M. S.; Smalley, R. E.; Wharton, L.; Levy, D. H. J. Chem. Phys. **1976**, 65, 1216.
- (23) Smalley, R. E.; Wharton, L.; Levy, D. H. J. Chem. Phys. **1978**, 68, 671.
- (24) Kubiak, G.; Fitch, P. S. H.; Wharton, L.; Levy, D. H. J. Chem. Phys. **1978**, 68, 4477.
- (25) Johnson, K. E.; Wharton, L.; Levy, D. H. J. Chem. Phys. **1978**, 69,

- 2719.
- (26) Sharfin, W.; Johnson, K. E.; Wharton, L.; Levy, D. H. J. Chem. Phys. **1979**, 71, 1292.
- (27) Kenny, J. E.; Johnson, K. E.; Sharfin, W.; Levy, D. H. J. Chem. Phys. **1980**, 72, 1109.
- (28) Blazy, J. A.; KeKoven, B. M.; Russell, T. D.; Levy, D. H. J. Chem. Phys. **1980**, 72, 2439.
- (29) Brinza, D. E.; Swartz, B. A.; Western, C. M.; Janda, K. C. J. Chem. Phys. **1983**, 79, 1541.
- (30) LeRoy, R. J.; Carley, J. S. In "Potential Energy Surfaces", K. P. Lawley, Ed.; John Wiley and Sons, Ltd.: New York, 1980.
- (31) Ewing, G. Chem. Phys. **1978**, 29, 253.
- (32) Beswick, J. A.; Jortner, J. Chem. Phys. Lett. **1977**, 49, 13.
- (33) Beswick, J. A.; Jortner, J. J. Chem. Phys. **1978**, 68, 2277.
- (34) Beswick, J. A.; Jortner, J. J. Chem. Phys. **1978**, 69, 512.
- (35) Beswick, J. A.; Delgado-Barrio, G.; Jortner, J. J. Chem. Phys. **1979**, 70, 3895.
- (36) Ewing, G. E. J. Chem. Phys. **1979**, 71, 3143.
- (37) Barrow, R. F.; Clark, T. C.; Coxon, J. A.; Yee, K. K. J. Mol. Spec. **1974**, 51, 428.
- (38) Coxon, J. A. J. Quant. Spectrosc. Radiat. Transfer **1972**, 12, 639.
- (39) Ng, C. Y.; Lee, Y. T.; Barker, J. A. J. Chem. Phys. **1973**, 59, 601.
- (40) Bettin, N.; Knockel, H.; Tiemann, E. Chem. Phys. Lett. **1981**, 80, 386.
- (41) Brinza, D. E.; Western, C. M.; Swartz, B. A.; Janda, K. C. To be

published.

- (42) Ng, C. Y.; Lee, Y. T.; Barker, J. A. J. Chem. Phys. **1974**, 61, 1996.
- (43) Coxon, J. A. J. Mol. Spec. **1971**, 32, 39.
- (44) Clyne, M. A. A.; Heaven, M. C. J. Chem. Soc., Faraday II **1978**, 74, 1192.
- (45) Beswick, J. A.; Delgado-Barrio, G. J. Chem. Phys. **1980**, 73, 3653.
- (46) Ewing, G. E. Faraday Discuss. Chem. Soc. **1982**, 73, 325.
- (47) Sharfin, W.; Kroger, P.; Wallace, S. C. Chem. Phys. Lett. **1982**, 85, 81.
- (48) Beswick, J. A.; Delgado-Barrio, G.; Villareal, P.; Mareca, P. Faraday Discuss. Chem. Soc. **1982**, 73, 406.

## APPENDIX I

### Design of Optics for Molecular Beam Laser-Induced Fluorescence Experiments

Molecular beam fluorescence experiments necessitate careful design of the optical system to maximize signal due to the low density of emitting molecules. In order to optimize the amount of light detected in fluorescence excitation and dispersed emission experiments, three optical subsystems must be designed with consideration of the characteristics of the laser excitation source, molecular beam apparatus, and the detection equipment. These subsystems are the excitation optics, the optics for collecting total fluorescence and the optics for collecting light which is to be frequency analyzed.

Figure 1 shows a schematic diagram of the apparatus. The excitation optical system consists of beam shaping and steering optics, focusing optics, and a window and baffle tube assembly to transfer the laser beam in and out of the molecular beam vacuum chamber while preventing scattered laser light from reaching the detectors. The optics for collecting fluorescence to be dispersed are a pair of lenses which efficiently couple the emitted light into a spectrometer with fixed light gathering power or etendue. The total fluorescence collection subsystem uses a low f-number lens to image the excited region of the molecular beam onto an adjustable set of slits. These slits are used to select the desired portion of the source to be transmitted to the immediately following photomultiplier tube detector and are also useful

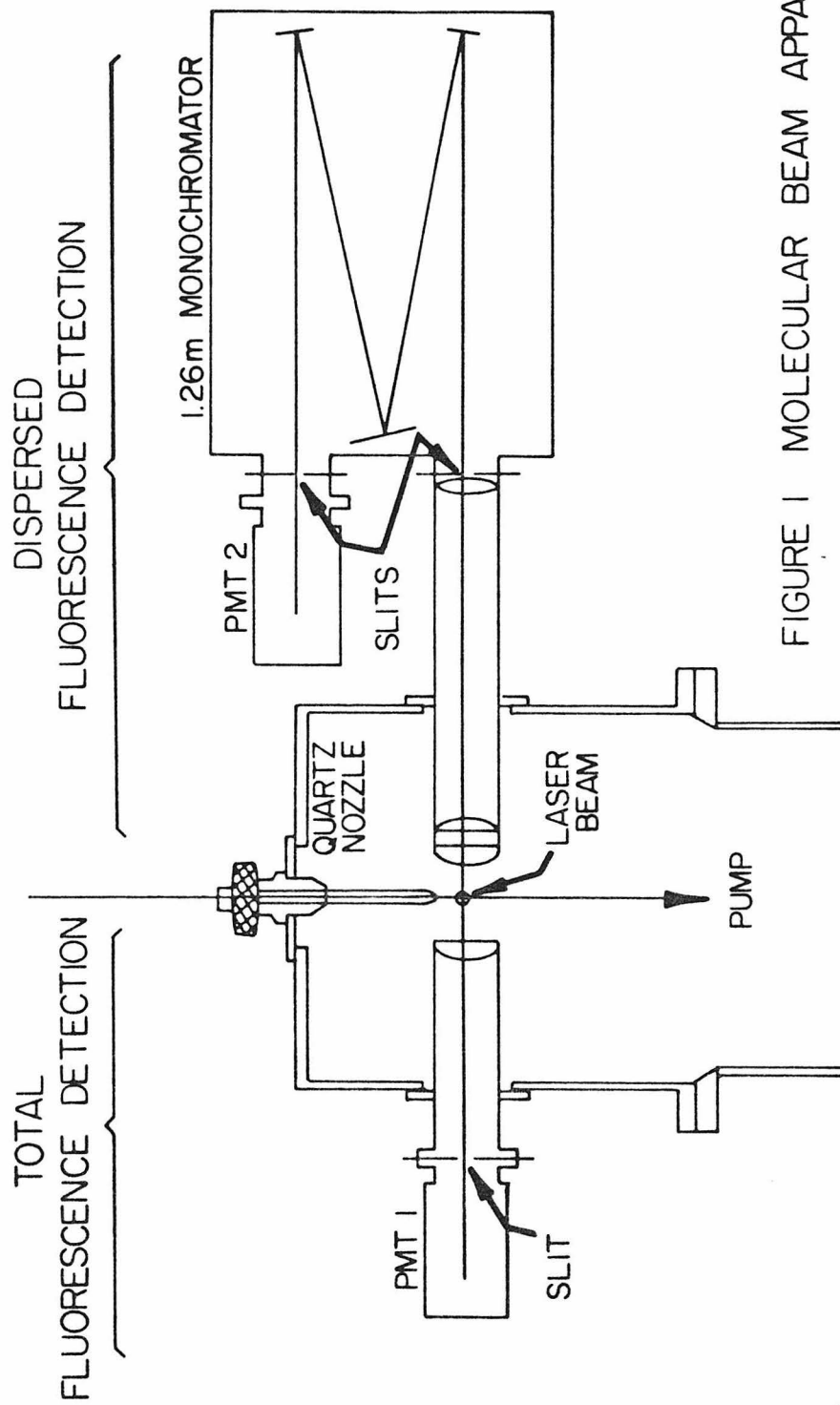


FIGURE 1 MOLECULAR BEAM APPARATUS

in eliminating scattered light.

It has been shown<sup>1</sup> that for light gathered from a gaseous sample which is Raman scattered or emitted from a transition which is not near saturation, optimum collection and spectrometer throughput is achieved if the exciting light is focused to form a source volume whose cross section has dimensions equal to the dimensions of the spectrometer slit image on the source. Thus, the excitation optics and the collection optics for dispersing fluorescence are strongly interrelated. The collection optics design is largely restricted by the fact that the spectrometer entrance slit must be located a minimum distance from the fluorescence source due to the width of the vacuum chamber combined with the distance from the chamber at which the spectrometer must lie to accommodate the photomultiplier detector at its exit slit. Also, the inclusion of resonant and near resonant total fluorescence detection capability in the system restricts the excitation focusing optics to be located outside the vacuum chamber at the end of a relatively long baffle tube.

This appendix will first calculate the etendue of a Spex 1269 spectrometer so that the dispersed fluorescence collection system may be insured to meet or exceed this light gathering power. Next, the focusing of the exciting laser beam to a focal volume which can be imaged on and passed by the spectrometer slits is discussed. The collection optics are then chosen to accomplish this with the required etendue while filling the spectrometer grating. The baffle tubes for elimination of scattered exciting light are then described. Finally, the total fluorescence collection lens is chosen.

For photoelectric detection, the etendue is an important factor in the

throughput of a spectrometer or other optical system which is given by<sup>2</sup>

$$\text{through flux} = kTB A_g \Omega \quad (1)$$

Here,  $k$  is a non-linear coefficient which approaches 1 for low resolution and accounts for such effects as slit diffraction.  $T$  is the transmission of the optical system, and  $B$  is the source luminescence at the wavelength of interest. The etendue,

$$e = A_g \Omega \quad (2)$$

is the product of the area of the limiting aperture,  $A_g$ , which, in the case of a spectrometer, is the grating area, times  $\Omega$ , the solid angle subtended by the slit area from the collimating mirror. In order to calculate the etendue for our SPEX 1269 spectrometer, one needs to refer to the fundamental grating equation for a Czerny-Turner monochromator,

$$m\lambda = d(\sin\alpha + \sin\beta) \quad (3)$$

where  $m$  is the order of diffraction,  $\lambda$  is the wavelength, and  $d$  is the grating spacing which is  $5.55 \cdot 10^{-4}$  mm for our 1800 grove/mm holographic grating, and  $\alpha$  and  $\beta$  are defined in Figure 2. This may be more conveniently written as

$$m\lambda = d(2 \sin\theta \cos\phi)$$

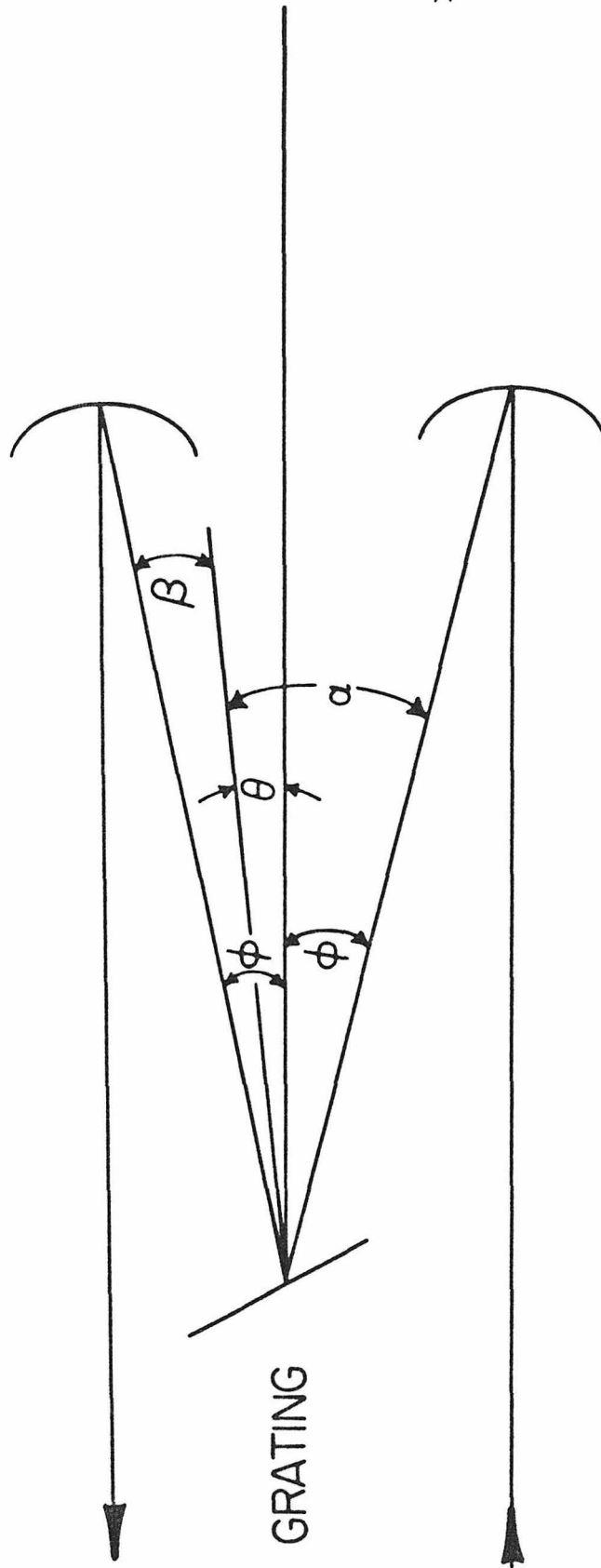


FIGURE 2 CZERNY-TURNER MONOCHROMATOR

or (4)

$$\theta = \sin^{-1} \frac{m\lambda}{2d \cos\phi}$$

where  $\theta$  and  $\phi$  are defined by the equations

$$\alpha = \theta + \phi$$

and (5)

$$\beta = \theta - \phi.$$

From Figure 2 it can be seen that  $\theta$  is the rotation of the grating from 0 degrees and that, for a given spectrometer,  $\phi$  is a constant and is equal to 4.9° in this case. The reciprocal angular dispersion is then given by

$$\frac{d\theta}{d\lambda} = \frac{1}{\cos\beta} \frac{m}{d} = \frac{(1800 \cdot 10^{-6})m}{\cos(\sin^{-1}(903.25 \text{ m}\lambda - 4.9))} \text{ nm}^{-1} \quad (6)$$

The grating area may be expressed as

$$A_g = H_g W_g \cos\beta \quad (7)$$

where  $H_g$  is the height and  $W_g \cos\beta$  is the projected grating width.  $\Omega$  can be written as

$$\Omega = W_s L_s / F^2$$

with (8)

$$W_s = F \Delta \theta .$$

$W_s$  and  $L_s$  are the slit width and length and  $F$  is the spectrometer focal length which equals 1260 mm. The etendue may then be written as

$$e = \left[ \frac{H_g W_g \cos \beta}{F} \quad \frac{\delta \theta}{\delta \lambda} \right] L_s \Delta \lambda \quad (9)$$

where  $\Delta \lambda$  is the bandpass and  $H_g$  and  $W_g$  equal 120 and 140 mm, respectively. The quantity in brackets in equation 9 is approximately constant over the wavelength range 300-1000 nm and equals  $24000 \pm 4$ . At the broadest bandpass anticipated of 1 angstrom,  $L_s$  equals 10 mm (slit width equals 0.25 mm) and the etendue is  $0.024 \text{ mm}^2$ . This is the figure of merit which must be met or exceeded by the collection optics for dispersed fluorescence.

To calculate the effects of beam shaping and focusing optics on the exciting laser beam it is necessary to examine the propagation of Gaussian optical beams in homogeneous and lenslike media. From Maxwell's equations, such a beam must satisfy the equation<sup>3</sup>

$$\nabla^2 \mathbf{E} + k^2 \mathbf{E} = 0 \quad (10)$$

where  $\mathbf{E}$  is the electric vector of the light and where  $k$ , the wave vector may

be limited to a radial dependence

$$k^2 = k^2 - k k_2 r^2 \quad (11)$$

where  $k_2$  is a constant. In a homogeneous medium  $k_2$  goes to 0 and the solution may be written

$$E(x, y, z, t) = \text{Re} \left\{ E_0 \frac{W_0}{W(z)} \left[ \exp \left( - i(kz - \omega t - \eta(z) - i \frac{kr^2}{2q(z)}) \right) \right] \right\} \quad (12)$$

with

$$\frac{1}{q(z)} = \frac{1}{R(z)} - i \frac{\lambda}{\pi n \omega^2(z)}$$

This is the form of a plane wave with  $1/e^2$  spot size of  $\omega(z)$  and radius of curvature  $R(z)$ . Here, the direction of propagation is assumed to lie along the  $z$  axis,  $\omega_0$  is the spot size at the beam waist at  $z = 0$ ,  $\omega$  is the angular frequency,  $n$  is the index of refraction, and

$$\eta(z) = \tan^{-1} \left( \frac{z}{z_0} \right) \quad (13)$$

with

$$z_0 = \frac{\pi \omega_0^2 n}{\lambda}$$

If  $k_2 \neq 0$ , as is the case for a lens, then

$$q(z) = \frac{\cos \sqrt{\frac{k_2}{k}} q_0 + \sqrt{\frac{k}{k_2}} \sin \sqrt{\frac{k_2}{k}} z}{-\sin \sqrt{\frac{k_2}{k}} z + \sqrt{\frac{k_2}{k}} q_0 + \cos \sqrt{\frac{k_2}{k}} z} \quad (14)$$

where

$$q_0 = \frac{i\pi\omega_0^2 n}{\lambda} \quad (15)$$

This has the form

$$q_2 = \frac{Aq_1 + B}{Cq_1 + D} \quad (15)$$

where A, B, C, and D are elements of the ray matrix characterizing the medium, and  $q_1$  and  $q_2$  are the input and output beam parameters, respectively, which fully characterize the propagating Gaussian beam.

Examples of ray matrices are:

propagation	$\begin{bmatrix} 1 & \ell \\ 0 & 1 \end{bmatrix}$	$\ell =$ distance of propagation
thin lens	$\begin{bmatrix} 1 & 0 \\ -1/f & 1 \end{bmatrix}$	$f =$ focal length of the lens
mirror	$\begin{bmatrix} 1 & 0 \\ -2/R & 1 \end{bmatrix}$	$R =$ radius of curvature of the mirror

The solution for simple propagation over a distance  $l$  is

$$q(l) = q_0 + l \quad (16)$$

from which it is found that

$$\omega(l) = \omega_0 \sqrt{1 + (l\lambda/\pi\omega_0^2)^2} \quad (17)$$

Problems involving one or two lenses are algebraically more involved. Therefore, the following computer program "Telescope", was written which, given the location and focal lengths of up to two lenses, calculates the position, spot size, and length of the waist formed in the beam.

```
PROGRAM TELESCOPE
C THIS PROGRAM CALCULATES THE RADIUS, WOUT, AND
C POSITION, L3, OF THE WAIST OF A LASER BEAM WHICH HAS AN
C INITIAL WAIST OF WIN AND GOES THROUGH FIRST A LENS WITH
C FOCAL LENGTH F1 AT L1 AND THEN A LENS WITH FOCAL LENGTH
C F2 AT L2 FROM L1 UNITS ARE CM AND L3 IS MEASURED FROM
C LENS 2
C REAL L2
40 WRITE(3,987)
987 FORMAT(' WIN=')
READ(3,9876)WIN
9876 FORMAT(F8.4)
WRITE(3,2345)
2345 FORMAT(' F1=')
READ(3,1235)F1
WRITE(3,345)
345 FORMAT(' F2=')
READ(3,235)F2
WRITE(3,2346)
2346 FORMAT(' L1=')
READ(3,1236)L1
WRITE(3,2347)
```

```

2347  FORMAT(' L2=')
      READ(3,1237)L2
      DO 100 I=3,10
      XLMDA=I*(1.0E-05)
      ZIN=(3.14159265*WIN*WIN)/XLMDA
      A3=(ZIN*ZIN*L2*F2*L2*L2*F2*+2*L2*(F1*F2-F1*F1*F2-F1*F2*
F2)-L1*CL1*L2*L2*F2+L1*L2*F2*F2+2*(L1*L1*L2+L1*L2*L2)*F1*F2-
(L1+L2)*C(L1+L2)*F1*F1*F2-(L1*L1+2*L1*L2)*F1*F2*F2+(L1+L2)*
F1*F1*F2*F2)/C(ZIN*ZIN*(2*L2*F1-L2*L2-F1*F1+2*L2*F2-F2*F2-2*
F1*F2)-L1*L1*L2*L2*C+2*(L1*L1*L2+L1*L2*L2)*F1+2*L1*L1*L2*F2-
(L1+L2)*(L1+L2)*F1*F1-CL1*L1*F2*F2-2*(L1*L1+2*L1*L2)*F1*F2+2*
(L1+L2)*F1*F1*F2+2*L1*F1*CF2*F2-F1*F1*F2*F2)
C      A3 IS ACTUALLY L3
      WOUT=((XLMDA/3.14159)*(ZIN**2*(L2*A3-A3*F1-(L2+A3)*F2+F1*
F2)**2+(C11*L2*A3-(L1*L2+L1*A3)*F2-(L2*A3+L1*A3)*F1+(L1+L2+A3)*
F1*F2)**2)/C(ZIN*((F1+F2-L2)*(L1*L2*A3-(L1*L2+L1*A3)*F2-(L2*
A3+L1*A3)*F1+(L1+CL2+A3)*F1*F2)+(L1*L2-L1*F2-(L1+L2)*F1+F1*
F2)*(L2*A3-A3*F1-(L2+A3)*CF2+F1*F2))))**0.5
      ZOUT=(3.14159*WOUT*WOUT)/XLMDA
      XLMDA=XLMDA*(1.0E 08)
      WRITE (3,1234)XLMDA, F1,F2,L1,L2,A3,WOUT,ZOUT
1234  FORMAT(' 0LAMBDA=',F6.0,3X,'F1=',F6.2,3X,'F2=',F7.2,3X,'L1=',13,3X,
C'L2=',F6.2/' L3=',E11.2,3X,'WOUT=',F10.5,3X,'ZOUT=',E11.2//)
      XLMDA=XLMDA*(1.0E-08)
1235  FORMAT(F6.2)
235   FORMAT(F7.2)
1236  FORMAT(13)
1237  FORMAT(F6.2)
100   CONTINUE
      GO TO 40
      END

```

For the case of a single focusing lens there is an approximate solution which is useful for intuitive understanding. Figure 3 defines the focal region parameters which are given by<sup>4</sup>

$$\begin{aligned}
 \alpha &= d/f \\
 b &= 8\lambda / (\pi\alpha^2) \\
 \omega_{\ell} &= \frac{2\lambda}{\pi\alpha} = \frac{2\lambda f}{\pi d}
 \end{aligned}
 \tag{18}$$

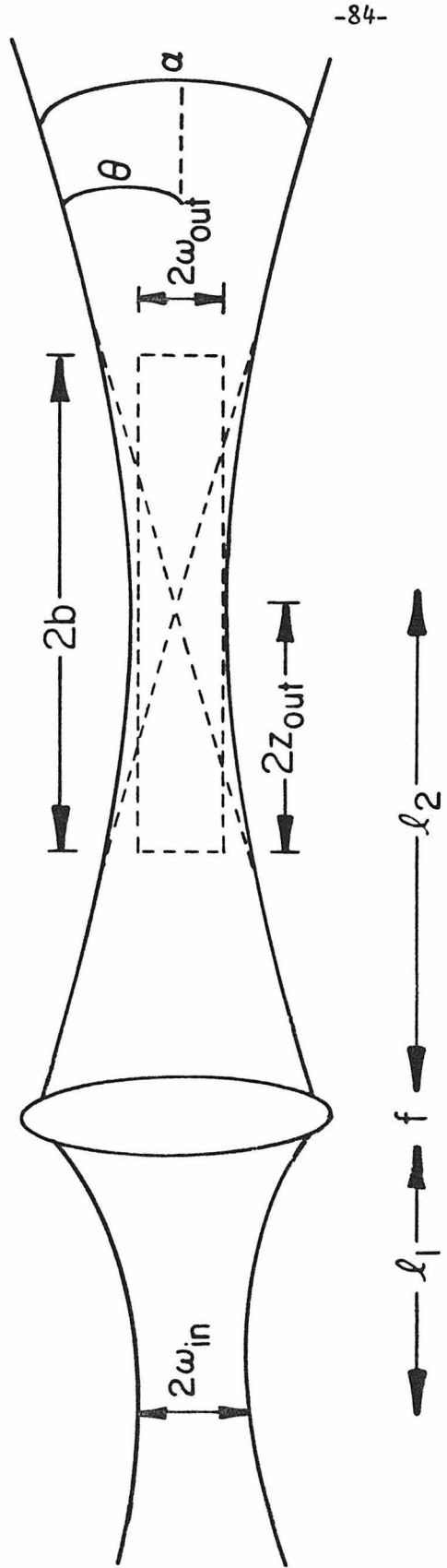


FIGURE 3 GAUSSIAN BEAM FOCUS

where  $d$  is the diameter of the beam at the lens. From this it can be seen that the shorter the lens focal length and the larger the initial beam diameter, the tighter the focus. The shortest focal length lens practical with our molecular beam apparatus is one with  $f = 50$  cm. With an input beam radius of 0.025 cm, which is the beam waist radius of our laser, and a laser to focusing lens distance of 100 cm, the 50 cm focusing lens produces a focal region 48 cm long and 0.04 cm in diameter. This is clearly too large to be imaged on and passed by the spectrometer entrance slit, especially if there is any magnification in the collection optics. The alternative, then, is to expand the laser beam using a telescope such that the diameter at the focusing lens is increased, producing a tighter focus. An achromatic telescope including a spatial filter was available in our laboratory. The telescope consists of a 1.28 cm focal length objective lens and a 20 cm focal length collimating lens which are spaced apart at a distance equal to the sum of their focal lengths. The spatial filter is a pinhole placed at the focus of the objective lens. This has the effect of eliminating stray light around the laser beam and insuring that the transverse mode of the laser beam has a Gaussian profile.

Using "Telescope" to calculate the effect of the telescope on the laser beam one finds that a beam with diameter 0.8 cm at the focusing lens is produced. With our 50 cm focal length focusing lens, this results in an excitation focal region with a diameter equal to 0.003 cm and a length of 0.44 cm. Thus, a magnification of eight in the collection optical system would result in just filling the 0.25 mm slit width of the monochromator. A 75 mm diameter doublet condenser lens with effective focal length of 75 mm

was chosen as the collection lens. Geometrical optics tells us that<sup>5</sup>

$$\frac{1}{f} = \frac{1}{S'} + \frac{1}{S''} \quad (19)$$

and

$$m = \frac{S'}{S''}$$

where  $f$  is the lens focal length,  $m$  is the magnification, and  $S'$  and  $S''$  are the image and object distances from the lens principal points, respectively. Using the fact that  $S' = 675$  mm for our arrangement yields a focal region to lens distance of 84 mm and a magnification of eight. The etendue of this collection system, calculated as the area of the focal region source times the area of the condenser lens divided by the square of the distance between them, is  $0.11 \text{ mm}^2$  which meets the requirement of exceeding the spectrometer etendue of  $0.024 \text{ mm}^2$ . It only remains to incorporate an appropriate field lens at the spectrometer slit to image the collection lens on the grating.<sup>6</sup> The grating is 140 mm tall so a magnification of 1.87 is needed to fill the grating with the collection lens image which insures the full realization of the spectrometer's resolving capability. Knowing that the spectrometer focal length is 1260 mm, equation 19 requires a lens of focal length 440 mm. This completes the design of the collection optics for dispersed fluorescence and leaves only the baffle tubes for the exciting laser beam and the total fluorescence collection system to be determined.

Figure 4 shows a diagram of the baffle tubes.<sup>7</sup> Apertures 1 and 2 are chosen to just pass the laser beam. Aperture 4 is chosen to pass the cone of

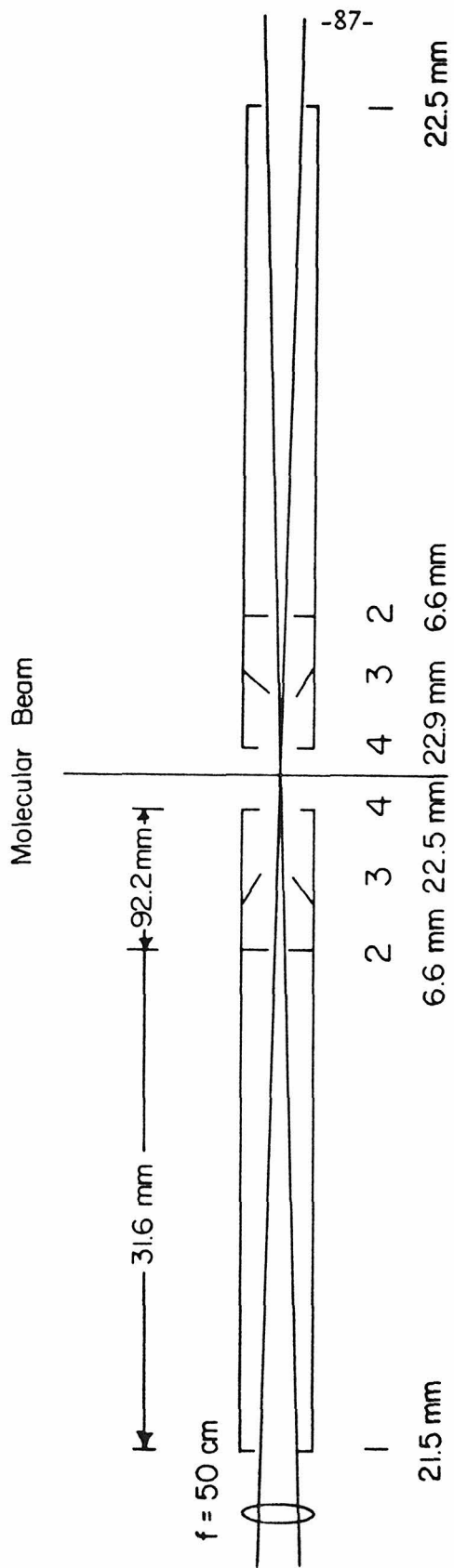


FIGURE 4 BAFFLE TUBES

scattered light defined by apertures 1 and 2. The angle of aperture 3 is determined by requiring not only that scattered light reflected off the cone hit the tube walls, but also strike the back side of aperture 4. Thus, scattered light must make many lossy reflections from surfaces which are black anodized before reaching the detection optics.

Integration of the Gaussian laser beam profile from 0 to  $d/2$ , where  $d$  is an aperture diameter, yields the expression for the fraction of laser power not passed through an aperture,  $f_{np}$ ,

$$f_{np} = e^{-d^2/2 \omega^2(z)}. \quad (20)$$

A diameter four times the laser spot radius,  $\omega$ , results in only  $10^{-4}$  of the laser power not being passed. "Telescope" was used to calculate the laser spot size along the baffle tubes and the diameters of apertures 1 and 2 were then chosen to be four times these spot radii. Aperture 1 was placed at the ends of the tubes and the position of aperture 2 was chosen so as to produce a scattered light cone whose diameter at aperture 4 was less than  $2/3$  of the baffle tube diameter. The diameters of apertures 3 and 4 were then determined by simple geometry.

The total fluorescence collection subsystem must collect as much light as possible from the source region and image it on a set of two dimensional slits located 300 mm from the source. The slits have a maximum length of 29 mm. An aspheric lens of diameter 75 mm and focal length 50 mm was chosen. Using equation 19 results in placing the lens 64 mm from the source

region, and produces an image on the slits at a magnification of 3.5. Using the length of the focal region previously calculated, the image at the slits is 24 mm long and is easily accommodated.

### References and Notes

- (1) Barrett, J. J.; Adams, III, N. I. J. Opt. Soc. Am. **1968**, 58, 311.
- (2) James, J. F.; Sternberg, R. S. "The Design of Optical Spectrometers"; Chapman and Hall, Ltd.: London, 1969.
- (3) Yariv, A. "Quantum Electronics"; John Wiley and Sons, Inc.: New York, 1975.
- (4) Benedek, G. B.; Fritsch, K. Phys. Rev. **1966**, 149, 647.
- (5) Born, M.; Wolf, E. "Principles of Optics"; Pergamon Press: Oxford, 1975.
- (6) Tobin, M. C. "Laser Raman Spectroscopy"; John Wiley and Sons, Inc.: New York, 1971.
- (7) Pruett, J. G. Zare, R. N. J. Chem. Phys. **1976**, 64, 1774.

## APPENDIX II

### Scanning Electronics for Coherent 699-03 Dye Laser

Continuous wave single frequency dye lasers offer the advantage of extremely narrow bandwidth radiation, but often with the drawback of having a very limited tuning range. Such is the case for the coherent model 699-03 single frequency ring dye laser in our laboratory which has a bandwidth less than 20 MHz while being tunable over only 6 GHz. It was therefore deemed necessary to increase this tuning range to greater than 30 GHz by the addition of appropriate scanning drives to the existing tuning elements.

Figure 1 shows a schematic diagram of the laser cavity. The input ion laser pump beam is focused by means of the pump mirror onto the gain medium which is a fluorescent dye in viscous solution circulated through a nozzle to form a laminar jet stream. The resonator is defined by four mirrors; the two high reflectors, the folding mirror, and the output coupler. This figure eight ring cavity has a round-trip length which results in a longitudinal cavity mode spacing of 280 MHz.

Lasing is restricted to single mode operation by three tuning elements (see Figs 2 and 3). First, the three-plate birefringent filter limits the lasing bandwidth to ~20 GHz. This is narrow enough to insure that lasing will be limited to a single mode of the 200 GHz free spectral range thin etalon. The thin etalon in turn limits the lasing bandwidth to allow lasing only within a single mode of the 10 GHz free spectral range thick etalon. The finesse of this thick etalon is then chosen to permit only a single cavity mode to lase.

FIGURE 1 CR-699-03 DYE LASER OPTICAL SCHEMATIC

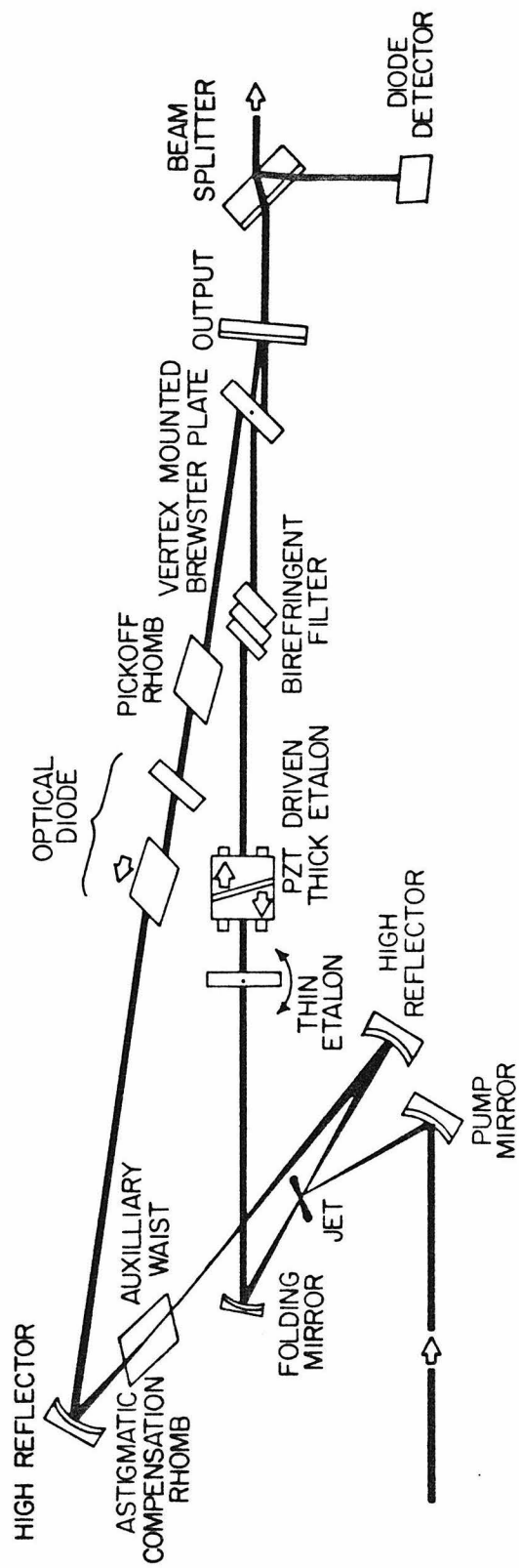
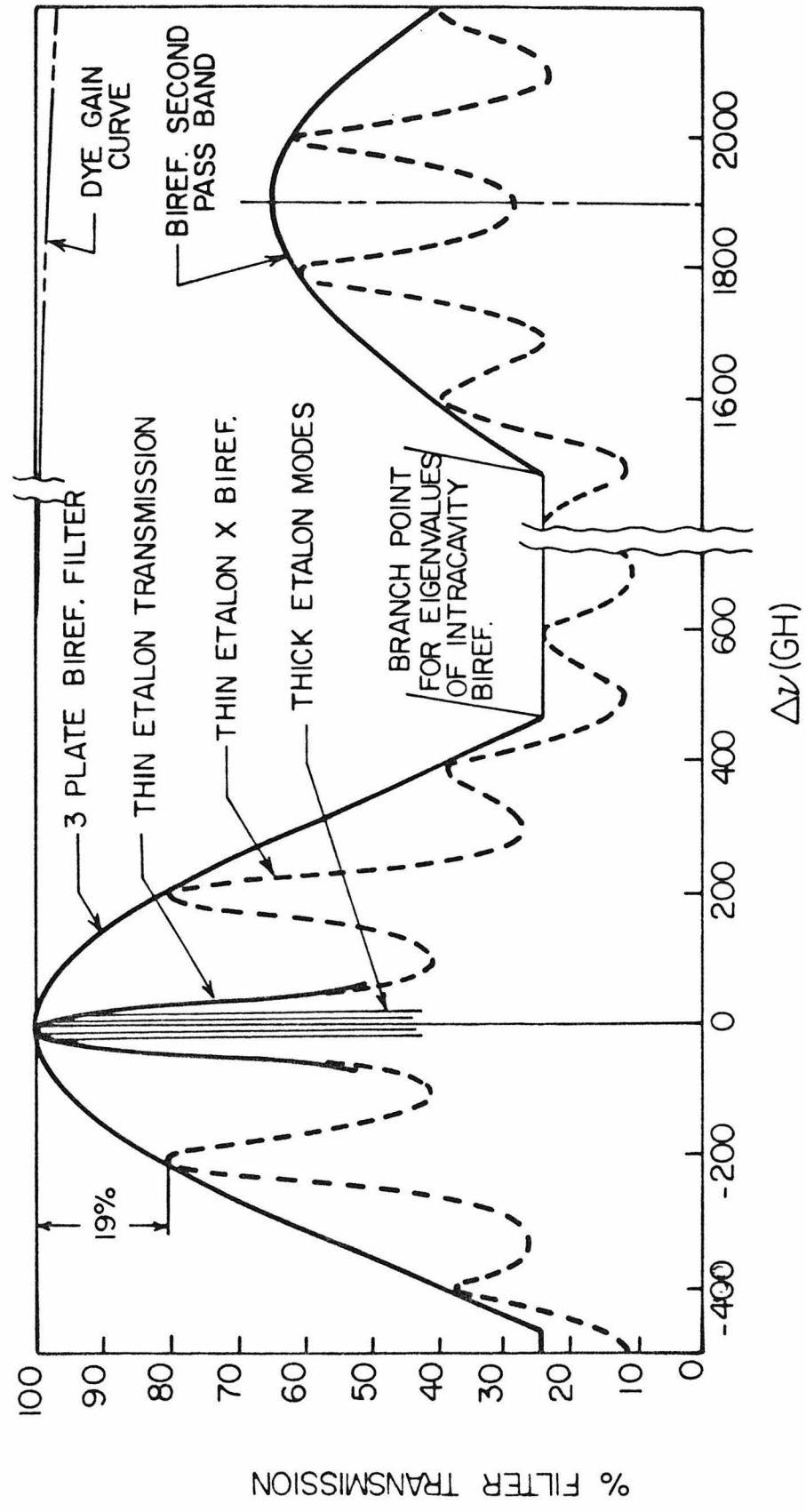


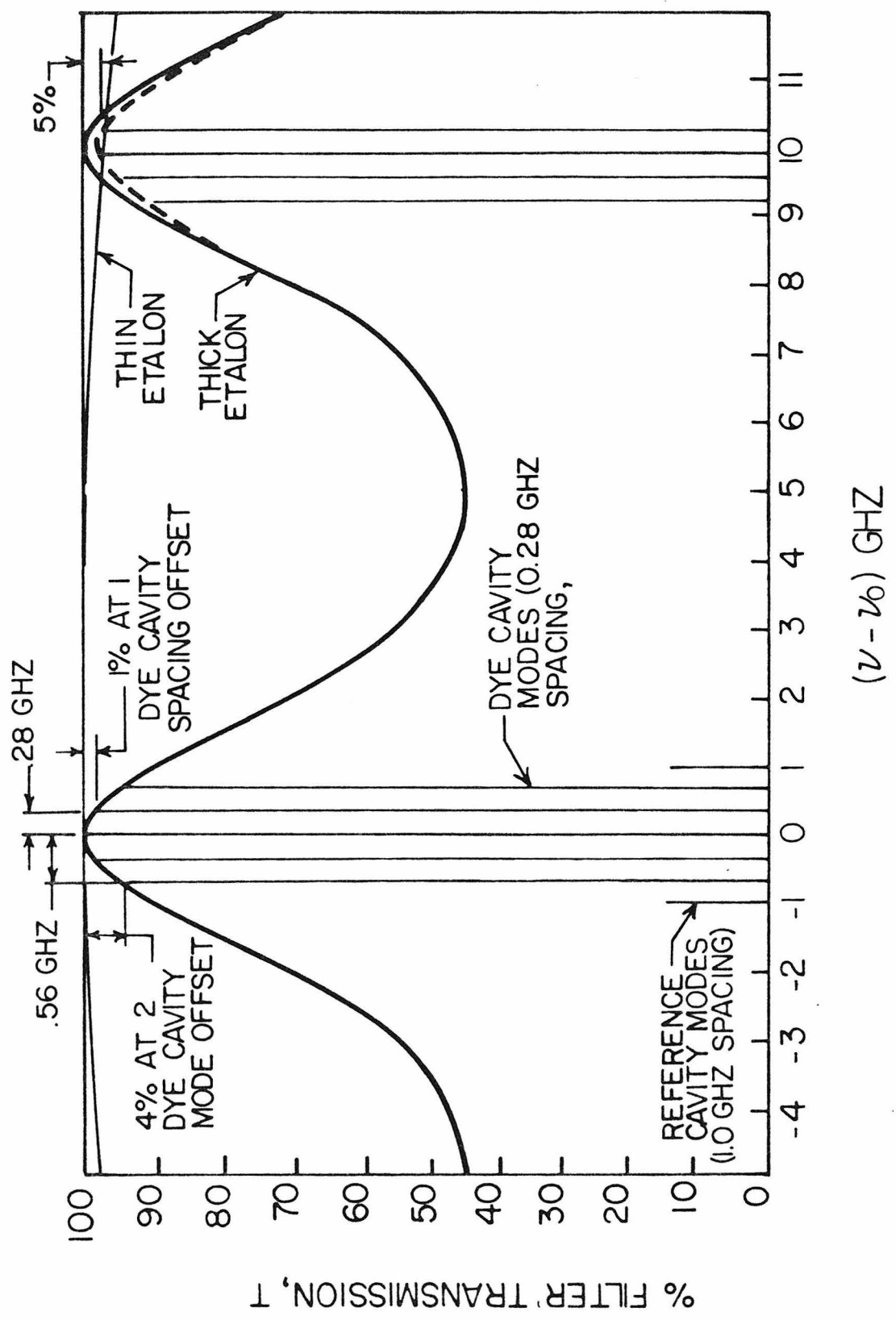
FIGURE 2 BIREFRINGEMENT FILTER AND THIN ETALON TRANSMISSION FUNCTIONS



% FILTER TRANSMISSION

$\Delta\nu$  (GH)

FIGURE 3 THIN AND THICK ETALON TRANSMISSION FUNCTIONS



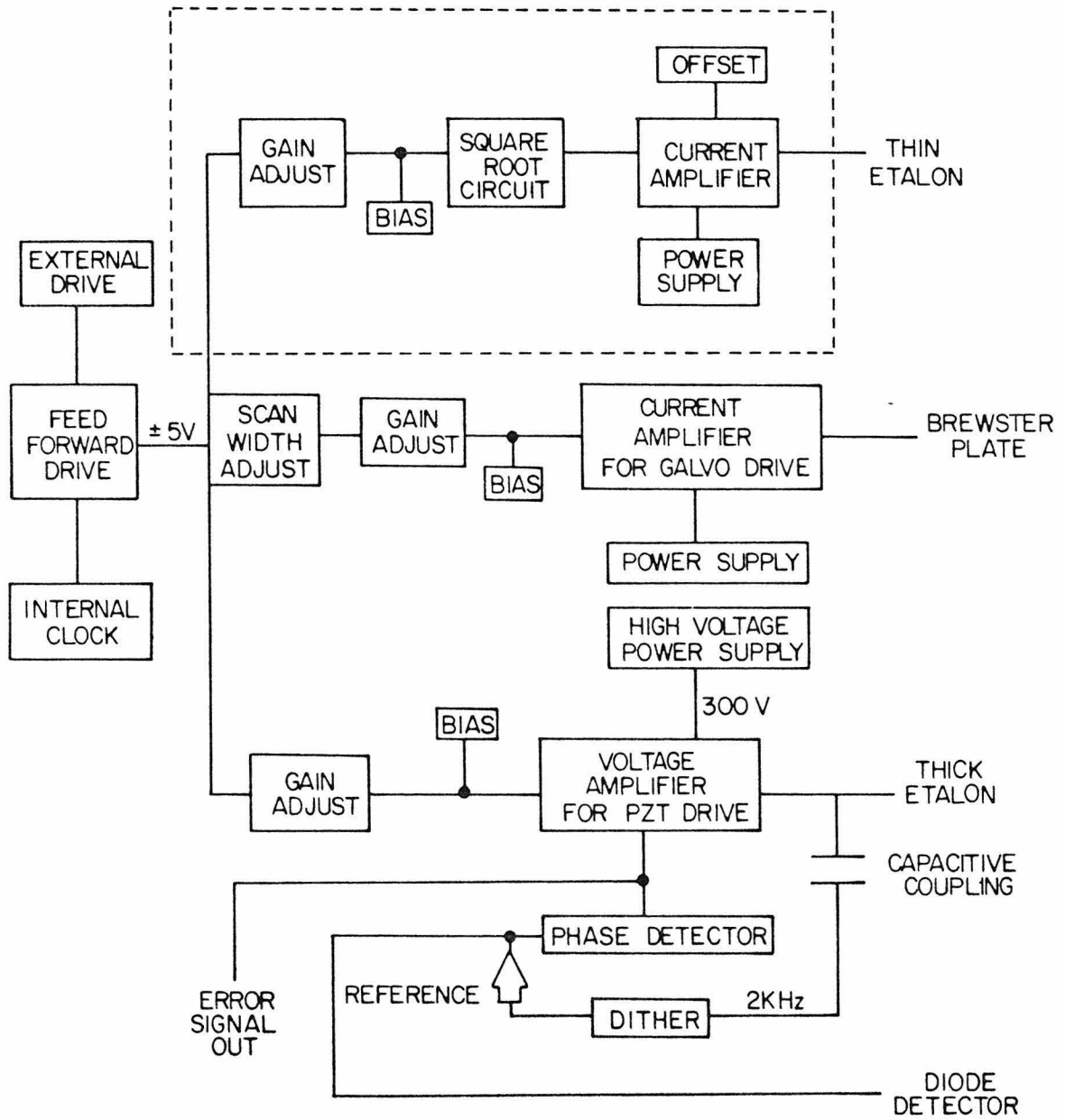
The optical diode ensures stable unidirectional operation.

Scanning of this single mode is achieved by means of a quartz plate mounted at Brewster's angle near the vertex of the cavity. Tipping of this plate by means of a galvanometer driver results via refraction in the continuous change of the cavity length, thus scanning the frequency of the oscillating mode. However, in order to prevent the lasing action from "hopping" to the next cavity mode, the thick etalon bandpass is scanned simultaneously by changing its thickness. This is accomplished by piezo-electric drivers which move the two Littrow prism halves of the thick etalon relative to each other. The length of the scan is then limited by the fixed thin etalon. Scanning further than 6 GHz results in a "hop" to the next thick etalon mode which has then shifted to the center of the thin etalon bandpass. It is thus necessary to include thin etalon scanning to increase the single mode tuning range.

It should be noted that the thin etalon in the model 699-03 is not actually fixed, but, rather, is manually tunable to allow setting the laser to a specific frequency. This points out a further drawback to the short 6 GHz scan width. It is not possible to make a long scan by simply piecing 6 GHz scans end to end. Tuning of the thin etalon results in a mode "hop" of the thick etalon of 10 GHz leaving a 4 GHz gap. Thus, it is even more imperative to provide continuous thin etalon scanning.

Figure 4 shows a block diagram of the 699-03 scanning electronics. The master feed forward drive controls the simultaneous scan of all the tuning elements. Gain adjusts for each element allow matching of individual scan lengths and the scan width adjust controls the total tuning range. Bias

FIGURE 4 699-03 SCANNING ELECTRONICS



controls adjust the absolute positions of the elements. The current amplifier for the Brewster plate is capable of a maximum of  $\pm 125$  mA. The sensitivity of the Brewster plate is 15.7 GHz/deg. rot. Its galvo driver has a sensitivity of 250 mA/deg. rot. yielding an overall sensitivity of 0.063 GHz/mA. The maximum Brewster plate scan range is thus 15.75 GHz. The voltage amplifier can produce a 0-100 V ramp with 0 bias. With a sensitivity in the piezo-electric transducers of 0.10 GHz/V, this leads to a thick etalon scan width of 10 GHz.

In addition to these scanning drives, a feedback loop is included. A small ac amplitude modulation at a frequency of 2 kHz is introduced onto the thick etalon voltage ramp. A small fraction of the output of the laser is detected by a photodiode. The amplitude of the ac component is then phase lock detected producing an error signal which is fed back to the voltage amplifier. This insures that the thick etalon bandpass remains centered on the scanning cavity mode. In addition, this error signal is extremely useful in the matching of the thick etalon and Brewster plate gains.

Clearly, then, three things must be done to increase the laser's scanning range. The Brewster plate current amplifier must be boosted. (The galvo driver is capable of handling  $\pm 750$  mA corresponding to 94.5 GHz.) The capability of the thick etalon voltage amplifier needs to be increased. (The piezo-electric transducers have a maximum input range of 0-500 V which would yield a 60 GHz scan width.) Finally, a drive to the thin etalon must be installed. The shift of the thin etalon bandpass with rotation is non linear. However, the response is closely approximated by a square root function. Therefore, a square rooting circuit must be incorporated into the feed

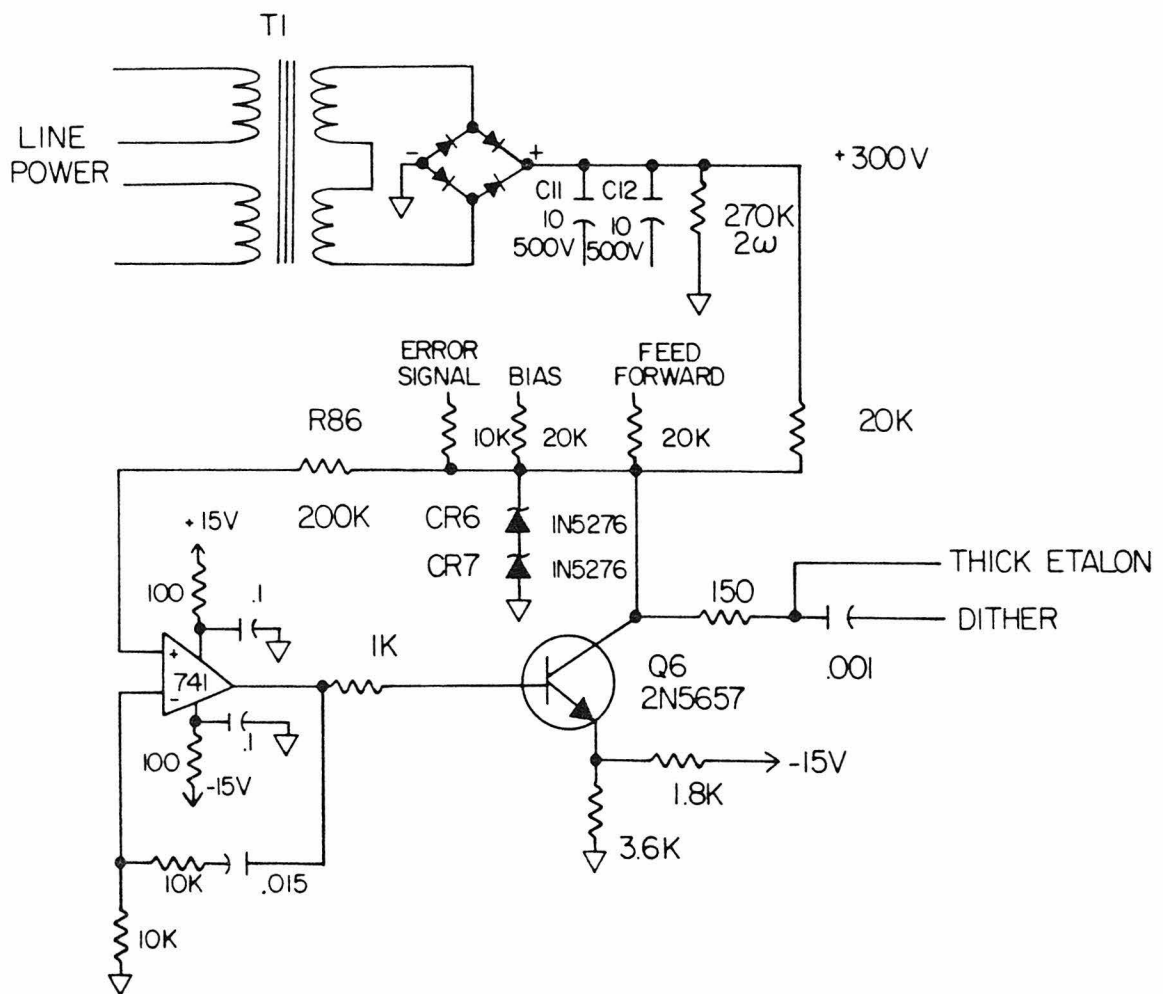
forward drive to an appropriate current amplifier and galvanometer driver.

The modification of the Brewster plate current amplifier is trivial. The feedback resistance in the amplifier is simply increased from 12 K $\Omega$  to 33 K $\Omega$  yielding an output of  $\pm 370$  mA corresponding to a scan width of 46.5 GHz.

Altering the thick etalon drive requires more work. A schematic diagram of the amplifier and power supply is shown in Figure 5. The supply voltage to Q6 is increased from the original 300 V by replacing T1 with a surplus transformer which produces 500 V dc output in the circuit. Also C11 and C12 are replaced with a 200  $\mu$ f filtering capacitor capable of withstanding 1000 V. The voltage rating of Q6 is not high enough to accommodate the increased power supply voltage so is replaced with an ECG 198 with  $V_{CBO} = 500$  V and  $V_{CES} = 500$  V. The 1/4 W R86 is replaced with a 2W 220 K $\Omega$  resistor to handle the increased current in the circuit. Also, another zener diode, an ECG 5166A, is added between CR7 and ground to prevent breakdown. These modifications result in a capability of producing an 8-430 V ramp with 20 V of usable bias which corresponds to a thick etalon scan range of 42 GHz.

The thin etalon is scanned using a General Scanning model Z-659 galvanometer optical scanner which has a sensitivity of 550 mA/deg. rot. The scanner is mounted directly on the existing thin etalon assembly without further modification. The sensitivity of the thin etalon is 0.529 $^\circ$ /10 GHz but, as previously mentioned, this is a square root function. Thus, a 20 GHz scan would require 0.75 $^\circ$  rotation and a 40 GHz scan necessitates a rotation of 1.06 $^\circ$  which corresponds to 583 mA of current through the galvanometer

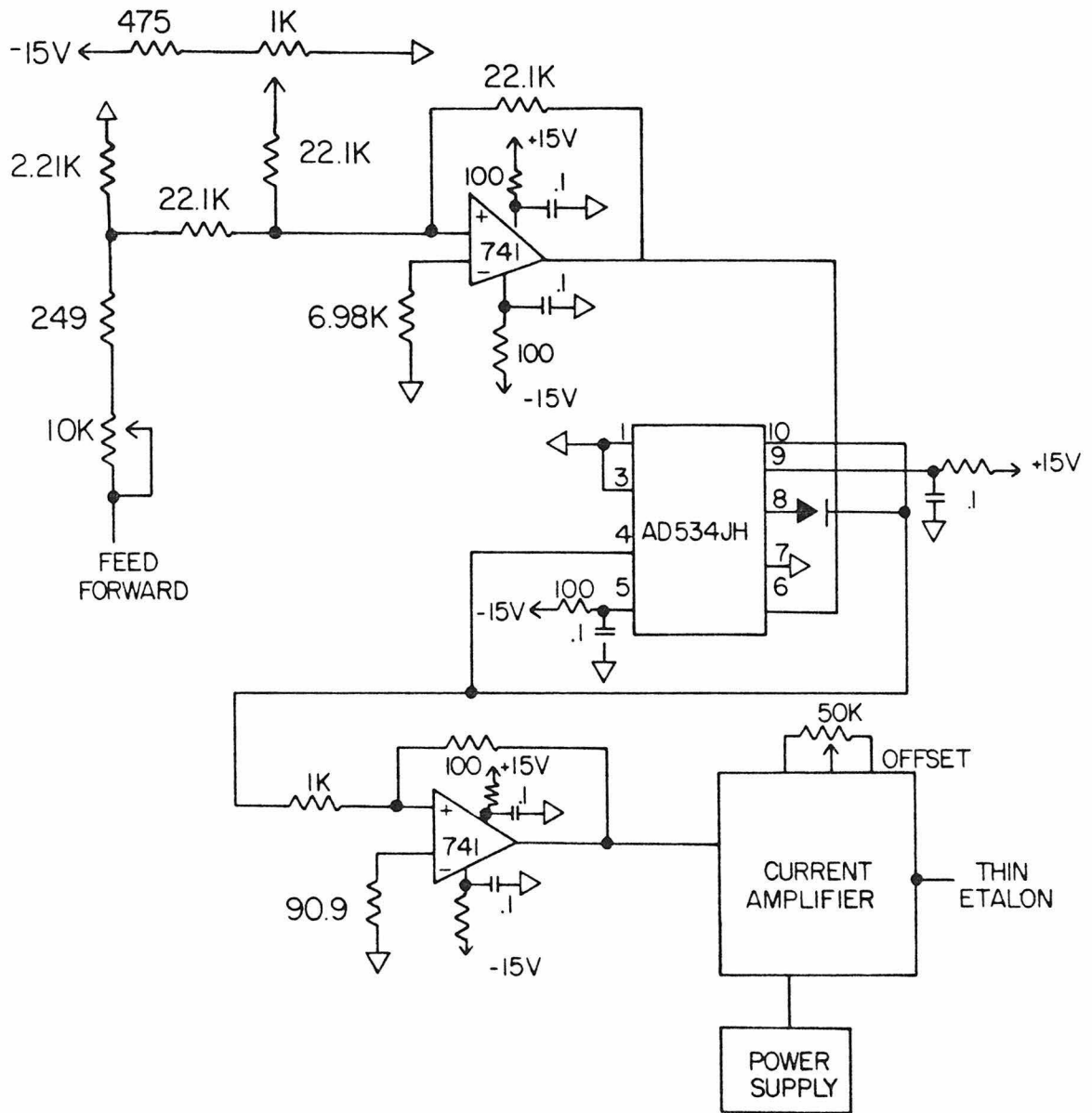
FIGURE 5 THICK ETALON VOLTAGE AMPLIFIER AND POWER SUPPLY



driver. Figure 6 shows a schematic diagram of the new thin etalon drive electronics. The current amplifier is a General Scanning model A-102 powered with a Power One power supply which delivers  $\pm 15$  VDC with 1.4 A. The amplifier accepts an input of  $\pm 1$  V to produce  $\pm 1.0$  A. The first amplifier stage offsets and sums the feed forward drive and bias. The  $>0$  output is then square rooted using an AD534JH multiplier chip configured for square rooting. The drive signal is amplified in the second amplifier stage to yield an input to the current amplifier of 0 V to 0.725 V over the feed forward range of  $\pm 5$  V. The current output then ranges from 0 to 725 mA producing a thin etalon scan capability of over 60 GHz.

All the tuning elements of the 699-03 are now capable of scanning greater than 40 GHz, so the laser now has a useful single frequency scanning range of over one wave number.

FIGURE 6 THIN ETALON DRIVE



### APPENDIX III

#### Design of a Spherical Mirror Fabrey-Perot Interferometer

High resolution spectroscopy using cw single mode dye lasers necessitates frequency analysis to high precision. Absolute wavelength determination may be accomplished with a wavemeter or a sufficiently high resolution spectrometer. However, it is also extremely useful to be able to provide reference frequency markers during a scan of the laser. A Fabrey-Perot interferometer with an appropriately chosen free spectral range can fill this need.

Although the tendency has been to use nonconfocal cavity interferometers for analysis of high resolution laser sources, the confocal arrangement offers certain advantages. It is much easier to use with cw laser sources due to its insensitivity to mode matching considerations, but suffers from an inability to easily alter the free spectral range because the mirror separation must be precisely defined. Also, mirror reflectivity limited resolution is readily achieved. A fixed free spectral range is not a serious drawback in this application, however, so a spherical mirror Fabrey-Perot interferometer was designed for our laboratory.

Connes<sup>1-3</sup> first described the spherical mirror Fabrey-Perot interferometer in some detail. Hercher<sup>4</sup> has more recently written a comprehensive description which is oriented to design considerations. The treatment here follows that of Hercher with considerations from Fork et. al.<sup>5</sup> and Polster.<sup>6</sup>

A spherical mirror Fabrey-Perot interferometer consists of two identical spherical mirrors separated by a distance  $r$  which is equal to their common radius of curvature. For a well collimated light source located on the interferometer axis such as a laser, a pattern of interference fringes is formed in the central plane of the interferometer by rays which intersect after multiple four transit paths. The fringes have radii  $\rho_m$  given by

$$\rho_m = (m\lambda r^3)^{1/4} \quad (1)$$

where  $m$  is the order of interference and  $\lambda$  is the wavelength of the light source. When this central fringe pattern is imaged on an aperture which selects the 0 order axial fringe spot, the instrumental band width,  $\Delta\nu_m$ , is given by

$$\Delta\nu_m = \Delta\nu_f / F \quad (2)$$

where  $F$ , the finesse, accounts for losses in the cavity and  $\Delta\nu_f$ , the free spectral range, is given by

$$\Delta\nu_f = c/4r \quad (3)$$

where  $c$  is the speed of light. Neglecting all but transmission losses at the mirrors, the finesse is given by

$$F = \pi R / (1 - R^2) \quad (4)$$

where  $R$  is the mirror reflectivity. To realize a resolving power  $\Delta\nu/\nu$  which is 70% of that corresponding to  $\Delta\nu_m$  of equation 2, the aperture spot size,  $\rho_s$ , must be

$$\rho_s = (r^3 \lambda / F)^{1/4} \quad (5)$$

The instrumental transmission,  $T_o$ , is given by

$$T_o = (1 + R^2) (T / (1 - R^2))^2 \quad (6)$$

where  $T$  is the mirror transmission.

Our modified Coherent 699-03 single mode dye laser operates with a bandwidth of less than 20 MHz over a wavelength range using rhodamine 6G and DCM dyes of 550-700 nm. It has a tuning range greater than 30 GHz. Therefore, an interferometer with  $r = 25$  cm and a resulting free spectral range of 300 MHz would provide convenient transmission marker peaks. A finesse of 52 is required to realize a bandpass of less than 6 MHz which corresponds to a reflectivity of 97% and an instrumental transmission of 44%. The limited availability of curved mirror substrates forced the purchase of quartz mirror substrates with  $r = 22.8$  cm from Spectra Physics, Inc. Appropriately separated, mirrors of this radii create an interferometer with  $\nu_f = 329$  MHz. Figure 1 is a transmission curve of the reflective

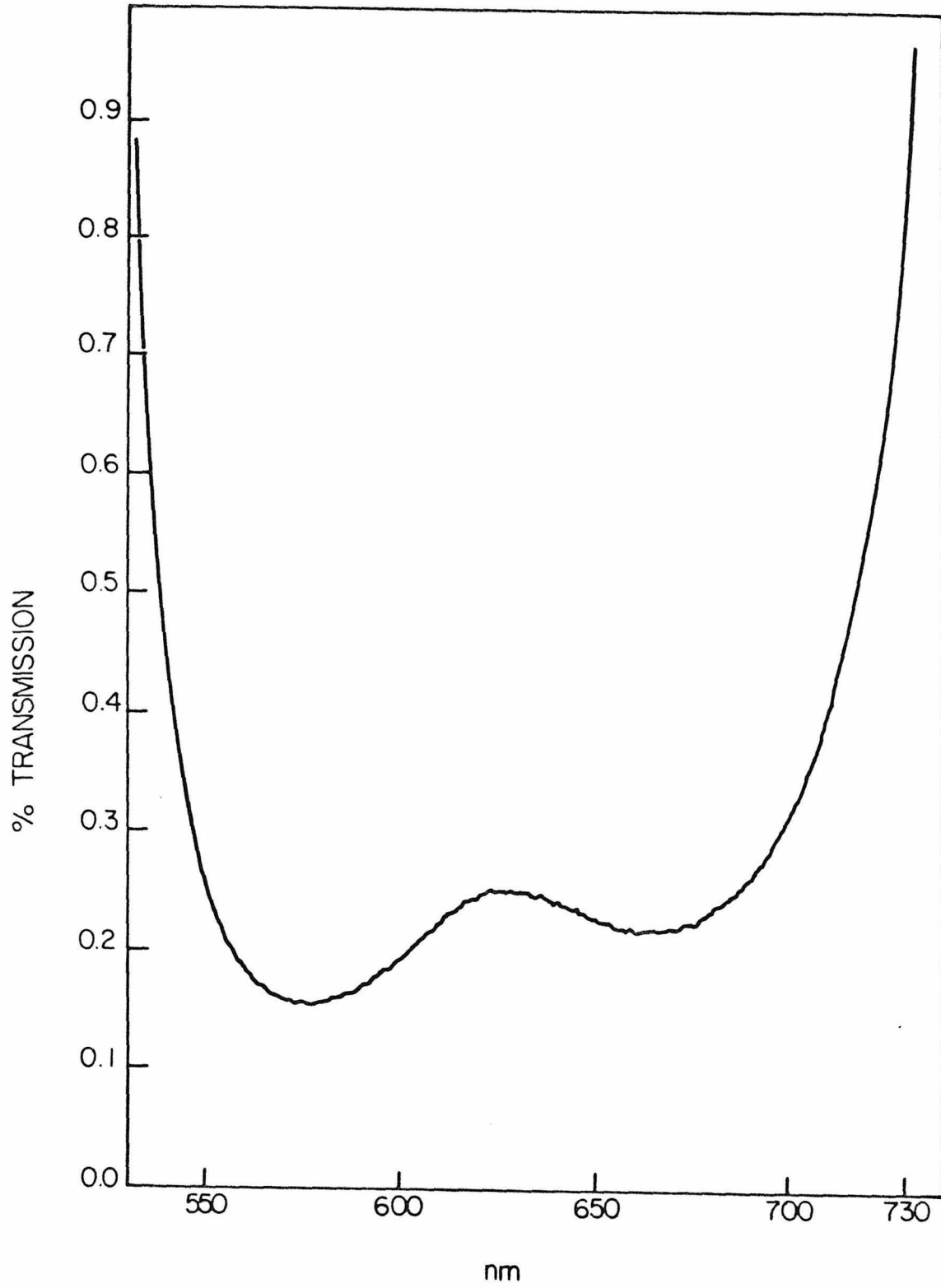


FIGURE I MIRROR TRANSMISSION

coatings applied to these substrates by Coherent Radiation, Inc. The average reflectivity of 97.5% over the large wavelength range of interest yields a finesse of 65 and an instrumental transmission of 42%. (Specified mirror losses are less than 0.02%.) This means that the bandpass is  $\sim 5$  MHz or  $\sim 1/4$  of the 20 MHz laser bandwidth. The value of  $\rho_s$  is then 1.0 mm, allowing the use of a photodiode detector.

The design of the interferometer must insure constant mirror spacing since a change in mirror separation of only  $\lambda/4$  scans through a full free spectral range. (Note that the free spectral range itself is relatively insensitive to very small changes in the mirror separation.) Materials with very low thermal expansion must, therefore, be used in the interferometer's construction.

Figure 2 is a diagram of the assembled interferometer. One of the mirror mounts allows for slight adjustment of the cavity length by means of a very fine thread to empirically determine the confocal arrangement using a reference frequency source such as a calibrated fluorescence signal. The spacer is machined from a rod of Zerodur which is a ceramic of low expansion manufactured by the Schott Glass Company. The particular piece used was molded from a melt with a thermal expansion coefficient of  $-0.02 \cdot 10^{-6}/^{\circ}\text{C}$ . The mirror mounts are made of super invar alloy with thermal expansion coefficient  $0.25 \cdot 10^{-6}/^{\circ}\text{C}$ . Thus, the appropriate combination of these materials, which is 21.11 cm of Zerodur and 1.69 cm of super invar, yields a 22.8 cm spaced interferometer for which the residual expansion is thermally compensated. The residual fractional change in mirror separation is then less than  $1 \cdot 10^{-9}/^{\circ}\text{C}$ . This is  $\sim 4\%$  of the wavelengths of interest per degree

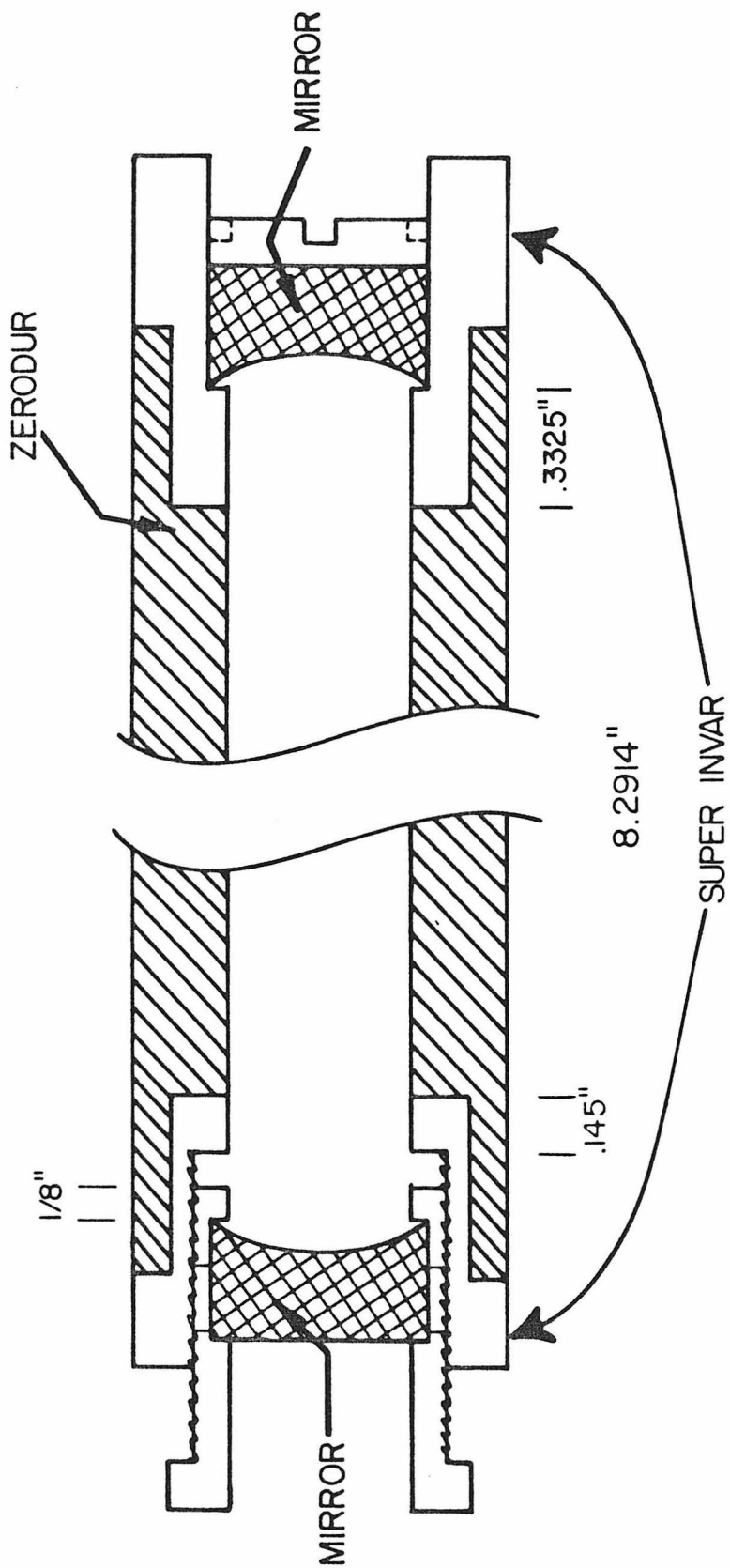


FIGURE 2 CONFOCAL ETALON

centigrade. Therefore, in a reasonably constant temperature environment, the interferometer provides stable frequency marks at 329 MHz intervals.

**References and Notes**

- (1) Connes, P. Rev. Opt. **1956**, 35, 37.
- (2) Connes, P. J. Phys. Radium **1958**, 19, 262.
- (3) Connes, P. In "Quantum Electronics and Coherent Light", P. A. Miles, Ed.; Academic Press, Inc.: New York, 1964, 0. 198ff.
- (4) Hercher, M. Applied Optics **1968**, 7, 951.
- (5) Fork, R. L.; Herriott, D. R.; Kogelnik, H. Applied Optics **1964**, 3, 1471.
- (6) Polster, H. D. Applied Optics **1969**, 8, 522.